Department of Precision and Microsystems Engineering

Topology Optimization of Metamaterials with Negative Linear Compressibility

Shawn Joseph D'Mello

Report no : 2024.039
Professor : Dr. Jun Wu, Dr. Ir. Lise Noël, Dr. Prabhat Kumar
Specialisation : Computational Design and Mechanics (CDM)
Type of report : M.Sc. Thesis
Date : 28 June 2024

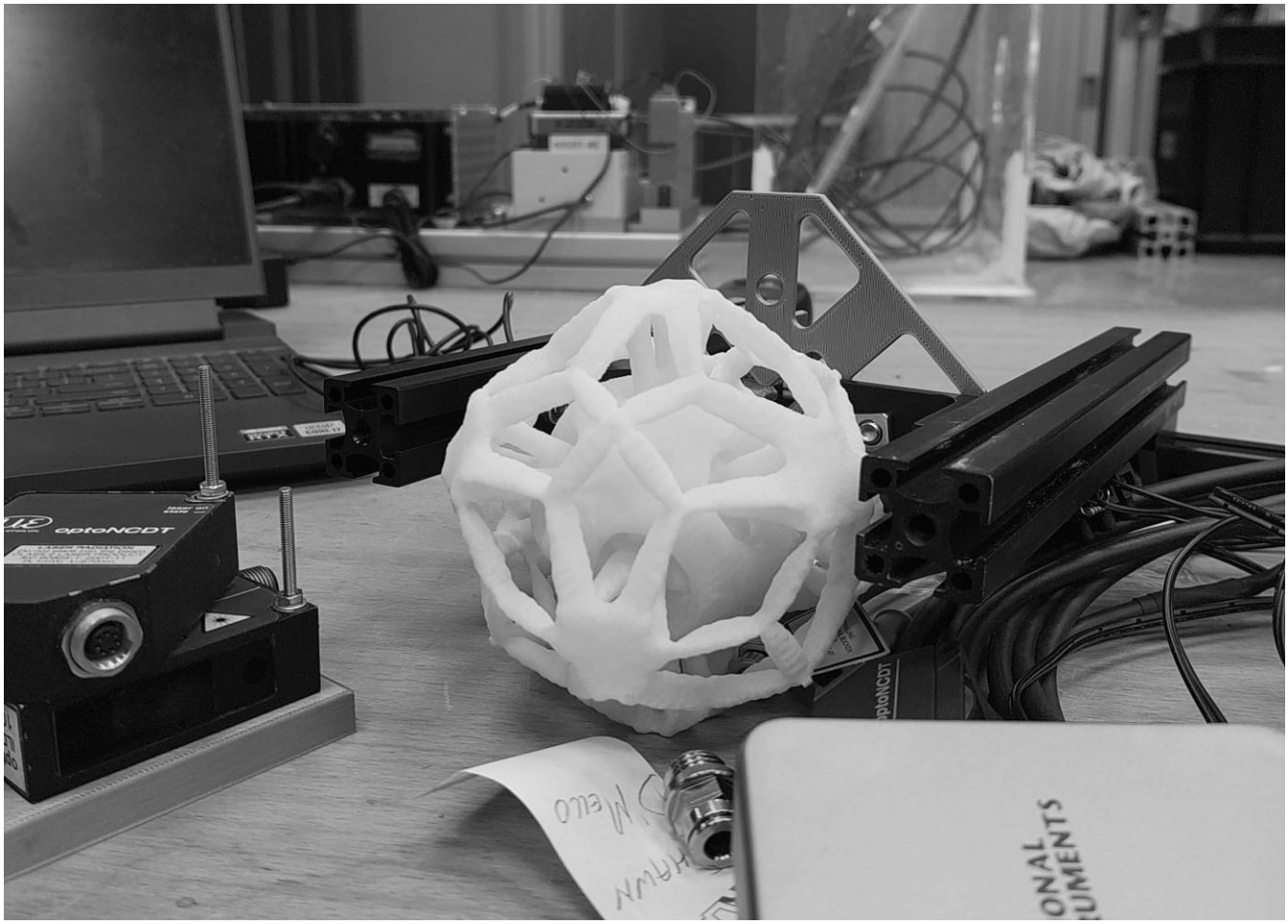

Topology Optimization of Metamaterials with Negative Linear Compressibility

by

Shawn Joseph D'Mello

to obtain the degree of Master of Science
at the Delft University of Technology,
to be defended publicly on Friday June 28, 2024 at 10:00 AM.

Student number:	5529670	
Project duration:	September 1, 2022 – June 28, 2024	
Thesis committee:	Dr. Jun Wu,	TU Delft.
	Dr. Ir. Lise Noël,	TU Delft.
	Dr. Prabhat Kumar,	IIT Hyderabad.

TU Delft

Abstract

Negative linear compressibility (NLC) describes the relative increase or decrease in a material's linear dimension when subjected to an increase or decrease in external pressure, or a decrease or increase in internal pressure, respectively. This is a rare material property found in only a few naturally existing materials. These materials are not only limited by their availability but also by the range, strength, and stability of NLC behavior. This limitation can be addressed through the design of NLC metamaterials, which are engineered materials composed of repeating architectures or material layouts on the microscopic scale, known as base or unit cells. These cells define the macroscopic properties of the material. In this case, negative linear compressibility.

While there are different methods for designing NLC metamaterials, none of them involve the use of topology optimization (TO), which serves as a powerful tool for designing optimized metamaterial structures. Materials can be designed for different parameters such as base material and pressure applied, while also considering different constraints that may be application-specific.

This study aims to create isotropic NLC metamaterials by designing NLC metamaterial unit cells using a systematic design methodology. We achieve this goal using a density-based TO approach, incorporating different constraints and selecting appropriate parameters to obtain different metamaterial unit cells that exhibit NLC behavior in both two and three dimensions.

The resulting 2D designs exhibited an NLC value of -2.370 %/bar and -3.367 %/bar. While the 3D designs exhibited an NLC value of -2.212 %/bar and -3.534 %/bar. The obtained NLC value and the efficacy of the design method are validated through numerical analysis and experimental testing, with the experimental design showing a maximum deviation of 26.099% from the NLC value obtained through TO. Finally, comparative and parameter studies helped better elucidate the advantages, limitations, and areas for improvement of the methodology used to obtain these designs.

Acknowledgements

Firstly, I would like to express my gratitude towards my supervisors: Professor Jun Wu, for not only introducing me to NLC metamaterials and providing me with a research topic to explore, but also for continuously guiding me through my research; Professor Prabhat Kumar, for his invaluable guidance and detailed explanations of the “Darcy Method”, as well as his substantial assistance in its implementation; and lastly, Professor Lise Noël, for her guidance and input, especially during the final stages of my thesis.

Secondly, I would like to thank some of the staff at TU Delft: Gideon Emmanuel, for providing me with the required tools to create my test setup; Spiridon van Veldhoven and Joris van Dam, for assisting me with the manufacturing of the design; and lastly, Jacques Brenkman, for providing me with the measurement tools.

Thirdly, I would like to thank my family and my friends: Matilde Garcia, Manabendra Das, Budhaditya Chakraborty, and several others, for constantly providing me with the necessary support and patiently assisting me whenever required.

Finally, I would like to acknowledge the use of computational resources of the DelftBlue supercomputer, provided by Delft High Performance Computing Centre (https://www.tudelft.nl/dhpc), for enabling me to run computationally expensive codes, and Oceanz BV for helping me realize my design through their manufacturing expertise.

Contents

1

Introduction

1.1. Background

Historically, there has always been an impetus to increase the capabilities of naturally occurring materials. While creating novel alloys and composites represent two significant methods to achieve this objective, a more recent approach (in the last two decades) involves the design of metamaterials. Metamaterials are artificially engineered materials that can be designed to exhibit exceptional properties usually not seen in nature. These materials, on the microscopic scale, consist of repeating architectures or material layouts known as base or unit cells that dictate the effective macroscopic properties of the material. Their unique or exceptional properties have been proven beneficial for various applications and have pushed the limits of traditional designs, leading to their increased popularity in recent years [1].

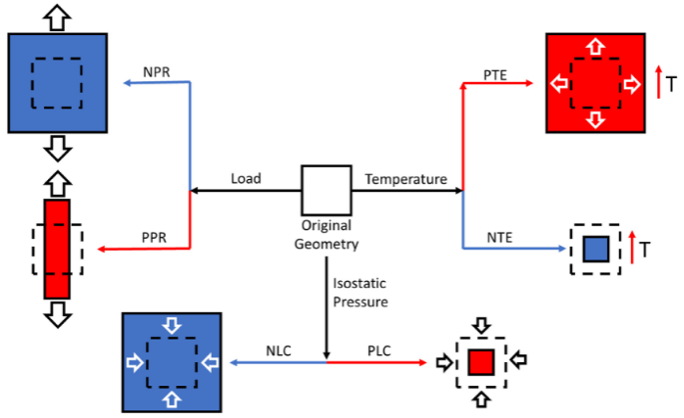

Figure 1.1: Schematic representation of different structural metamaterial behaviors. Negative Poisson's ratio (NPR) metamaterials expand/contract laterally when a tensile/compressive force is applied. Similarly, negative coefficient of thermal expansion (NTE) metamaterials contracts/dilates when heat is applied/removed from the metamaterial. Finally, negative linear compressibility metamaterials contract/expand when the external pressure is decreased/increased. Most naturally existing materials exhibit the behaviors of their positive counterparts, positive Poisson's ratio (PPR), positive coefficient of thermal expansion (PTE), and positive linear compressibility (PLC), respectively [2, 3].

Negative Linear Compressibility (NLC) is one such exceptional property that can be engineered through the design of mechanical metamaterials, which are a subset of metamaterials focused on manipulating the mechanical properties of the overall material. NLC, along with negative Poisson's ratio (NPR) and negative coefficient of thermal expansion (NTE), are three of the most studied properties in structural metamaterials [3]. While several publications concerning the design of NPR [4, 5] and NTE [6] exist, the development of NLC metamaterials is still in the early exploratory phases [7, 8]. The behavior of materials with these three mechanical properties and their positive counterparts are illustrated in Fig. 1.1.

1.2. Negative Linear Compressibility

Compressibility is a broader physical property of a material that is defined as the relative change in dimensions of that material under a change in external pressure. This can further be specified as either volume compressibility, area compressibility, or linear compressibility; where the definition describes the relative change in volume, area, or length of the material respectively. Negative volume compressibility is observed when the volume of the material either increases/decreases when there is an increase/decrease in external pressure. It is important to note that negative volume compressibility does not guarantee NLC along all three axes. A material may have a large NLC along one axis but may show small positive linear compressibility values along the other two axes leading to an overall negative volume compressibility of the material. This can better understood through Fig. 1.2.

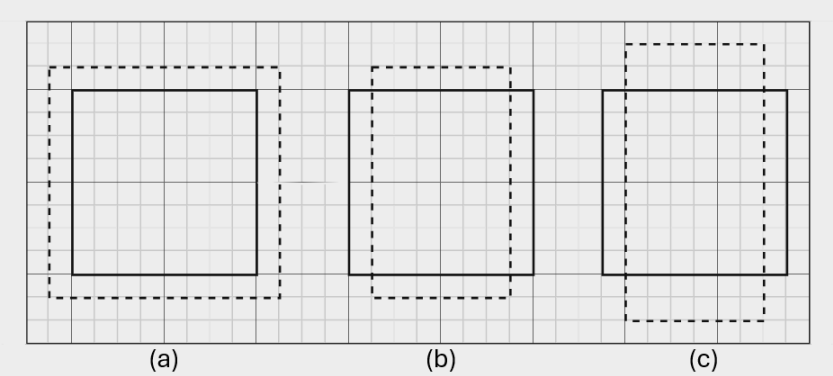

Figure 1.2: Schematic representation of different area compressibility (AC) cases. Dotted line describes the shape after external pressure is applied. **(a)** Negative AC with NLC in the two directions. **(b)** Positive AC with NLC in one direction and PLC in the other. **(c)** Negative AC with NLC in one direction and PLC in the other. Similar cases can be observed for volume compressibilities.

In this study, the focus will be on designing NLC metamaterials that exhibit isotropic compressibility; thereby demonstrating equal NLC along all three axes. Consequently, an NLC metamaterial with isotropic linear compressibility would imply that the material also possesses negative volume and negative area compressibility values. It is also important to note that the definition of NLC in metamaterials differs from the normal definition. Since NLC metamaterials are made up of base cells, their length-/area/volume is defined in terms of effective length/area/volume. This is illustrated in Fig. 1.3, where the area of the highlighted unit cell is defined in terms of its side length while the effective area is defined in terms of its side length and the thickness of the base material.

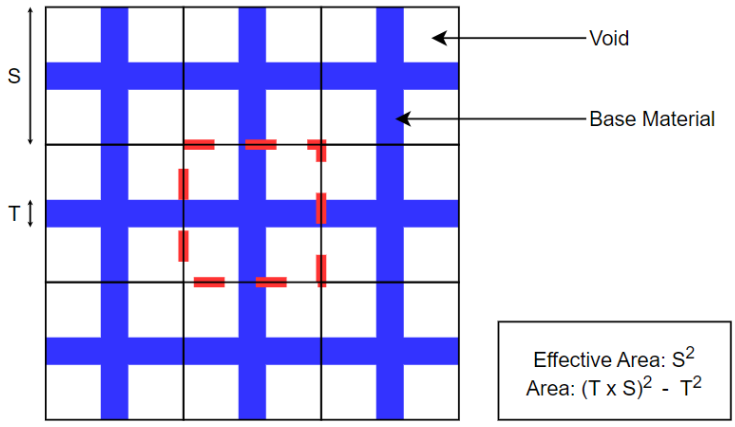

Figure 1.3: Schematic representation of the difference between effective area and area. Similarly, effective length and effective volume can be defined.

Mathematically, the compressibilities are defined as [9]:

$$\left.\begin{aligned} K_L &= -\tfrac{1}{L}\left(\tfrac{dL}{dP}\right)_T \\ K_A &= -\tfrac{1}{A}\left(\tfrac{dA}{dP}\right)_T \\ K_V &= -\tfrac{1}{V}\left(\tfrac{dV}{dP}\right)_T \end{aligned}\right\}, \tag{1.1}$$

where K_L denotes linear compressibility along one axis of length L, K_A, the areal compressibility across a face of area A, and K_V, the volume compressibility of the volume V; all when exposed to a change in pressure dP at a constant temperature T. Variables dL, dA, and dV denote the change in length, area, and volume, respectively.[1]

1.3. Negative Linear Compressibility Materials

NLC is a rare material property that was first observed in tellurium [10]. However, further reviews, first by Baughman et al. [9] and later by Cairns and Goodwin [11], listed 13 and 30 materials, respectively, that showed some level of NLC behavior. A more recent study by Miller et al. [12] presented 38 materials that show NLC behavior, including some common materials like polyvinyl chloride (PVC) and paper, which seemingly solved the problem of the availability of NLC materials. However, they are still limited by their inherent range, strength, and stability of compressibility and tend to be impractical when it comes to use in most engineering applications. This has led to a focus on developing NLC metamaterials that can be tuned and optimized to overcome the disadvantages of naturally existing NLC materials. Lim [13] compiled existing NLC metamaterial designs and broadly classified them into three types of systems: cellular, bi-material strip, and interconnected membrane. While some methods show NLC along only one direction, others are capable of showing NAC and even NLC along multiple orthogonal directions. While there exist a number of different NLC architectures, which can be select according to specific application requirements, the designs are still limiting, and a systematic methodology is required to design NLC metamaterial that are tailored to their intended application.

1.4. Metamaterial Design

NLC metamaterials belong to a class of metamaterials known as structural metamaterials [3]. A structural metamaterial at its core is made up of repetitive base cells in the microscopic scale. These cells can be made up of a structure or a solid mechanism that determines the overall structural properties of the metamaterial [14]. While many past base cell designs have relied on the intuition and experience of scientists and engineers, a systematic design approach is imperative when it comes to taking full advantage of metamaterials. There are different systematic design approaches that can be used to design these base cell structures or mechanisms. However, compliant mechanism (CM) design proves to be a better design approach when compared to traditional rigid body mechanism design [15]. This is because CMs possess the following advantages:

1. They do not require assembly: CMs that are fully flexible (obtaining all their motion from flexible components) do not require assembly, this is beneficial for metamaterials for two reasons. First, the unit cells of metamaterials are on the microscopic scale which makes the assembly difficult. Second, metamaterials consist of repetitive unit cells, making the assembly process tedious.
2. Possibility of monolithic designs: This makes it easy to manufacture with different microscopic scale manufacturing techniques, which is important when it comes to manufacturing metamaterials.
3. They are wear free: They eliminate friction as there are no contact surfaces between two parts, this leads to larger motion cycles and an overall larger life cycle.
4. They are precise: CMs are wear free, friction free and backlash free which leads to highly precise motion which is important in metamaterials to prevent any errors which could build up due to the large number unit cells.

CM design involves many different methods and techniques. Gallego and Herder [16] enlisted different CM synthesis techniques that could be used to design metamaterials. A chart of the different synthesis

1 For metamaterials, the length, area and volume in the compressibility equation will be replaced with effective length, area and volume.

techniques is illustrated in Fig. 1.4.

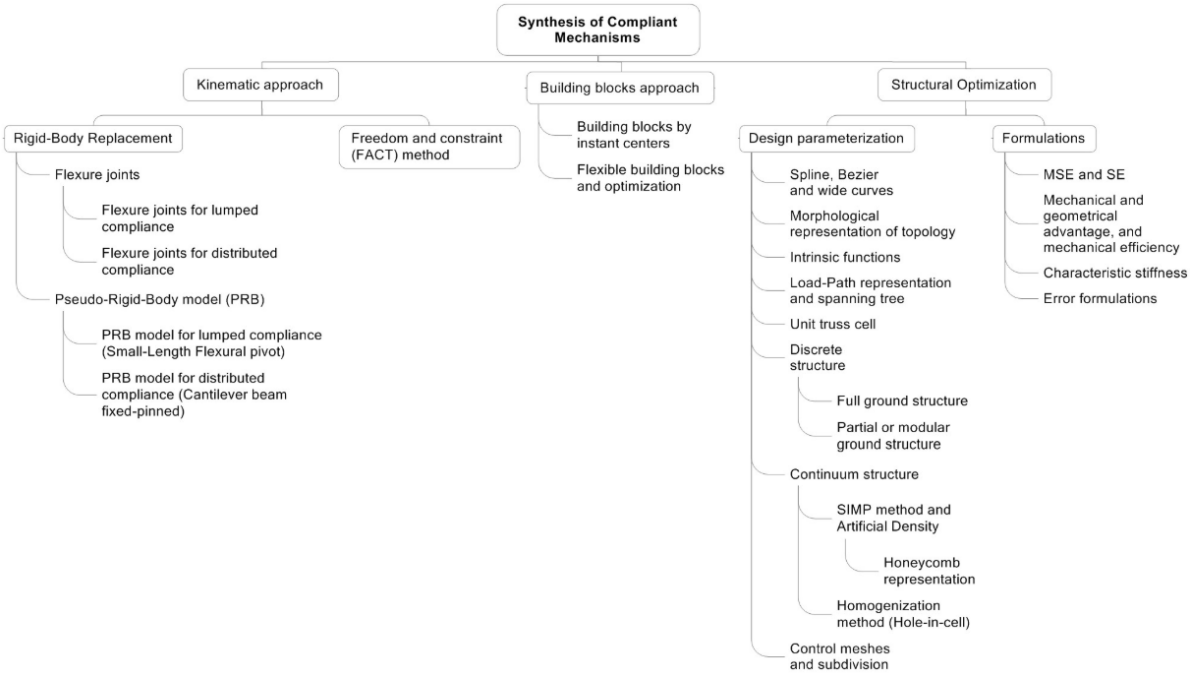

Figure 1.4: Chart of different CM synthesis methods [16].

Structural optimization, more specifically TO proves to be a suitable design method because of the systematic approach and great design freedom it possesses. This is particularly helpful when it comes to designing metamaterials, the reasons behind it are:

1. Maximizing or minimizing the objective: TO is able to provide either the highest or lowest possible index value. For example, maximizing the Poisson's ratio for PPR metamaterials or minimizing the linear compressibility value for NLC metamaterials.
2. Obtaining symmetry: Different TO techniques and/or constraints can be used to obtain symmetric results which could be used to obtain isotropic metamaterials.
3. Manufacturing limitations: Manufacturing limitations can be taken into account using constraints including adding passive regions and by complying to a minimum length scale. This is important for metamaterials as the base cells are designed for the microscopic scale and the manufacturing techniques in the microscopic scale have a lot of limitations.
4. Failure criteria: Constraints can be added to ensure that the design satisfies a predefined failure criteria, which is obtained from the type of material used, the loading condition experienced and the application it is used for. Typically, most metamaterials are required to undergo plenty motion cycles and are thereby required to have a high fatigue-resistance.
5. Optimizing for material: Designs obtained through TO are dependent on material properties and therefore every material possess a unique design which is optimized for its properties.

1.5. Topology Optimization

Pioneered by Bendsøe and Kikuchi [17] through a homogenization based approach, TO is a mathematical method through which the material distribution in a design space can be optimized, for either a specific performance or property value (also known as the objective function). This is achieved by applying specified loads, boundary conditions and constraints. Most algorithms use a finite element (FE) method to calculate the objective function and this step is repeated till the desired objective function value is achieved. The material layout differs in every step, and changes according to an optimization algorithm. The optimality criteria (OC) method and the method of moving asymptotes (MMA) are two such optimization algorithms that help push the current material layout towards the optimized layout.

A popular approach to TO is density-based TO, which uses the elemental densities as the design variables and aims to achieve a material density layout that minimizes the objective function while satisfying all the constraints. The material space in a density-based TO is discretized into elements each of which have an initial density value. The density value in these elements are linked to a certain material property of their respective elements. These densities change through an iterative penalization method that penalizes the material properties in each element, till the optimal material layout is obtained [18]. This iterative change in density values can be observed in Fig. 1.5. Simplified isotropic material with penalization (SIMP) approach is a common material interpolation and penalization method used in many structural optimization problems, as it relates the design variables to the elemental elasticity modulus E_e. The equation for E_e in terms of elemental density ρ_e can be written as:

$$E_e(\rho_e) = E_{\text{min}} + \rho_e^{\gamma}(E_0 - E_{\text{min}}), \tag{1.2}$$

where E_0 is the Young's modulus of solid material, E_{min} is the Young's modulus of the void material and γ is the penalization factor.

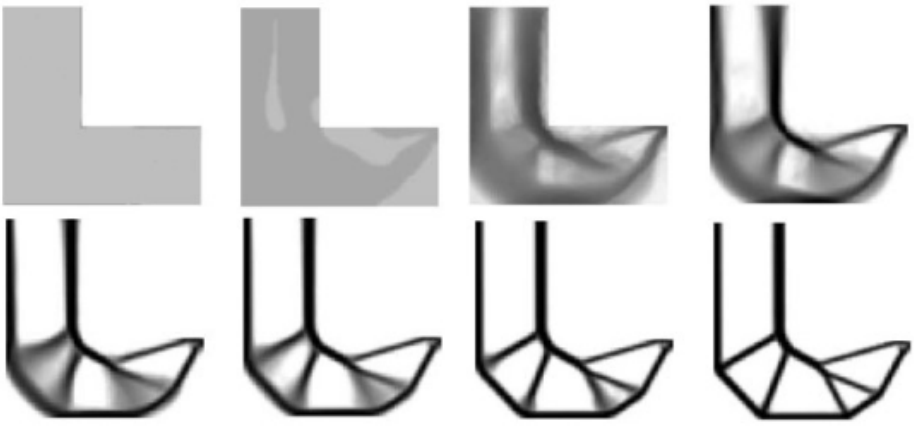

Figure 1.5: The design evolution for a compliance minimization problem using density-based TO. The first design is the initial material space and the final design is the optimized design.

1.6. Research Goal and Motivation

The goal of this research is to establish a systematic design methodology using TO for the design of NLC unit cells. The established method should be capable of creating tailored NLC metamaterial designs, that can be used in various applications.

The motivation behind this research is to advance the development of NLC metamaterials, given their numerous existing and potential applications. For example:

1. NLC metamaterials can be implemented similarly to NPR metamaterials, creating programmable metamaterials and active mechanical metamaterials [19, 20].
2. A combination of NLC and PLC can be used to create superior hybrid metamaterials [21] or even provide actuation. An example of actuation that could be achieved with NLC and PLC metamaterials is a soft robotic arm.
3. There are also applications that solely utilize the NLC property exhibited by these metamaterials, such as pressure sensors and actuators [9].
4. Lastly, materials exhibiting both NLC and NPR behavior are exceptionally suited for damping mechanisms, including soundproofing, protective devices (car bumpers, seismic protection), and biomedical applications (stents, skin grafts, smart dressings, and implants) [22].

1.7. Outline

The initial focus of this report, Section 2, will be a comprehensive literature review, beginning with an exploration of the currently established NLC metamaterial designs. This will be followed by an examination of two methods of metamaterial design using TO. The final part of the literature review will focus on the various TO methods that can tackle design-dependent pressure loads[2]. The literature review will elucidate the rationale behind using TO as an NLC metamaterial design process, the most suitable method of metamaterial design using TO for NLC metamaterials, and an optimal approach for addressing design-dependent pressure loads.

These insights will then inform the subsequent section, Section 3, the methodology, which will include a detailed explanation of the design process and its validation methods namely, numerical analysis and experimental analysis.

Section 4, the results and discussion, will present and explain the designs obtained from the methodology. The section will also provide a relative difference between the NLC values obtained from TO and the NLC values obtained through the validation methods. The section concludes with a parameter study comparing the influence of certain TO design parameters on the final NLC value. It also includes two comparative studies: one testing whether the NLC behavior of the obtained design is superior to a state of the art design, and the other evaluating the importance of the pressure load application method in a design-independent context.

Finally, Section 5, the conclusion and future scope, will summarize the results, detail the findings, describe the importance of the findings, and discuss the future scope of the study, including areas of research that would help better understand and establish the design methodology.

2 Pressure loading in TO is tricky as the pressure boundary where the load is applied can change as the design evolves, this means that the pressure load is design-dependent.

2

Literature Review

2.1. Negative Compressibility Metamaterials

Compressibility can be defined in terms of linear, area and volume compressibility, as denoted in Eq.1.1. This equation can be used to find the three linear compressibilities [13], as shown in Eq. 2.1.

$$\left.\begin{aligned} \alpha_1 &= -\left(\frac{\varepsilon_1^1+\varepsilon_1^2+\varepsilon_1^3}{dp}\right)_T \\ \alpha_2 &= -\left(\frac{\varepsilon_2^1+\varepsilon_2^2+\varepsilon_2^3}{dp}\right)_T \\ \alpha_3 &= -\left(\frac{\varepsilon_3^1+\varepsilon_3^2+\varepsilon_3^3}{dp}\right)_T \end{aligned}\right\}, \tag{2.1}$$

where the linear compressibility is denoted by α while the linear strain corresponding to the change in pressure dp under constant temperature T is denoted by ε. The subscripts denote the direction of strain and the superscript denotes the direction of load application. The three directions correspond to the three orthogonal directions along the coordinate axes. The change in pressure dp is equal to the applied stress σ in the orthogonal directions denoted by the superscript.

$$\sigma^1 = \sigma^2 = \sigma^3 = dp, \tag{2.2}$$

Negative volume compressibility does not guarantee negative area compressibility along all three orthogonal planes nor does it guarantee NLC along all three orthogonal directions. Therefore, the definition of a negative compressibility (NC) metamaterial is broad and can be used for a material that shows either negative compressibility linearly along at least one direction or areally along one of the orthogonal planes defined by two directions, or in terms of the volume of the metamaterial. Lim [13] compiled different negative compressibility metamaterials that exhibit either negative linear, area or volume compressibilty and broadly classified them into three types of systems: cellular, bi-material strip, and interconnected membrane. Most of these metamaterials are porous in nature and allow fluid to easily pass through the system, thereby applying pressure evenly on all surfaces. Note: The pressurized fluid passes through and the metamaterial system but not through the base material, for enclosed holes in the 2D case, fluid is allowed to pass over the material bounding it and into the empty space. However, enclosed voids in the 3D case do not allow fluid to pass through.

2.1.1. Cellular System

The metamaterial designs put forth by Grima et al. [23, 24, 25, 26], Attard et al. [27], Zhou et al. [28, 29], Ma et al. [30], Dudek et al. [31], and Grima-Cornish et al. [32] fall into the category of cellular systems. The change in unit cell dimensions of these metamaterials is defined by either the amount of stretching or rotation the rib of the unit cell undergoes. Sometimes it is also a function of both stretching

and rotation. These three cases are visualised in Figs. 2.1, 2.2, and 2.3. The unit cells can be defined as [13]:

$$\left.\begin{aligned} X_1 &= X_1\left(l_1, l_2, \ldots, l_m, \theta_1, \theta_2, \ldots, \theta_n\right) \\ X_2 &= X_2\left(l_1, l_2, \ldots, l_m, \theta_1, \theta_2, \ldots, \theta_n\right) \\ X_3 &= X_3\left(l_1, l_2, \ldots, l_m, \theta_1, \theta_2, \ldots, \theta_n\right) \end{aligned}\right\}, \tag{2.3}$$

which is a function of rib lengths l and inclination angles θ. m and n define the total number of ribs and inclination angles, respectively. The linear compressibilities of the cellular NC metamaterial systems can be derived by calculating the individual strains from Eq.2.3 which can then be used to derive the linear compressibilities as done in Eq.2.1. Cellular systems can further be divided into three categories depending on the major cause of deformation in the metamaterial.

Rib Stretching Mode

These are cellular systems where the strain is solely a function of the rib lengths. They are designed as either a network of rods/ribs joined at the junctions with pin joints, to allow free rotation about the hinges without incurring bending moment, or as a network of rods/ribs joined at connectors that permit only sliding translational motion. As a result, the equation for the strains is simplified and can be noted as:

$$\left.\begin{aligned} \varepsilon_1^1 &= \frac{1}{X_1}\left(\frac{\partial X_1}{\partial l_1} dl_1^1 + \frac{\partial X_1}{\partial l_2} dl_2^1 + \ldots + \frac{\partial X_1}{\partial l_m} dl_m^1\right) \\ \varepsilon_2^1 &= \frac{1}{X_2}\left(\frac{\partial X_2}{\partial l_1} dl_1^1 + \frac{\partial X_2}{\partial l_2} dl_2^1 + \ldots + \frac{\partial X_2}{\partial l_m} dl_m^1\right) \\ \varepsilon_3^1 &= \frac{1}{X_3}\left(\frac{\partial X_3}{\partial l_1} dl_1^1 + \frac{\partial X_3}{\partial l_2} dl_2^1 + \ldots + \frac{\partial X_3}{\partial l_m} dl_m^1\right) \\ \varepsilon_1^2 &= \frac{1}{X_1}\left(\frac{\partial X_1}{\partial l_1} dl_1^2 + \frac{\partial X_1}{\partial l_2} dl_2^2 + \ldots + \frac{\partial X_1}{\partial l_m} dl_m^2\right) \\ \varepsilon_2^2 &= \frac{1}{X_2}\left(\frac{\partial X_2}{\partial l_1} dl_1^2 + \frac{\partial X_2}{\partial l_2} dl_2^2 + \ldots + \frac{\partial X_2}{\partial l_m} dl_m^2\right) \\ \varepsilon_3^2 &= \frac{1}{X_3}\left(\frac{\partial X_3}{\partial l_1} dl_1^2 + \frac{\partial X_3}{\partial l_2} dl_2^2 + \ldots + \frac{\partial X_3}{\partial l_m} dl_m^2\right) \\ \varepsilon_1^3 &= \frac{1}{X_1}\left(\frac{\partial X_1}{\partial l_1} dl_1^3 + \frac{\partial X_1}{\partial l_2} dl_2^3 + \ldots + \frac{\partial X_1}{\partial l_m} dl_m^3\right) \\ \varepsilon_2^3 &= \frac{1}{X_2}\left(\frac{\partial X_2}{\partial l_1} dl_1^3 + \frac{\partial X_2}{\partial l_2} dl_2^3 + \ldots + \frac{\partial X_2}{\partial l_m} dl_m^3\right) \\ \varepsilon_3^3 &= \frac{1}{X_3}\left(\frac{\partial X_3}{\partial l_1} dl_1^3 + \frac{\partial X_3}{\partial l_2} dl_2^3 + \ldots + \frac{\partial X_3}{\partial l_m} dl_m^3\right) \end{aligned}\right\}. \tag{2.4}$$

The Greek letter ε denotes the different strains induced in the direction denoted by the subscript due to a load in the direction denoted by the superscript. The strains are a function of the unit cell dimension X and the rib lengths l. Finally, m denotes the total number of ribs.

Fig. 2.1 describes an example of a 2D system exhibiting NLC as a result of rib stretching. This system displays NLC behavior in one of the two orthogonal directions when the external pressure is reduced. This system is porous and allows fluid to pass through the system. The system in the figure experiences NLC behavior in the Ox_1 direction but positive linear compressibility in the Ox_2 direction.

Rotational Mode

The strain of rotational cellular systems are only a function of the inclination angles. The deformation of these systems are caused by the rotation of rigid ribs or the rotation of rigid units. Similar to the rib-stretching mode, the equation for the strains can simplified as:

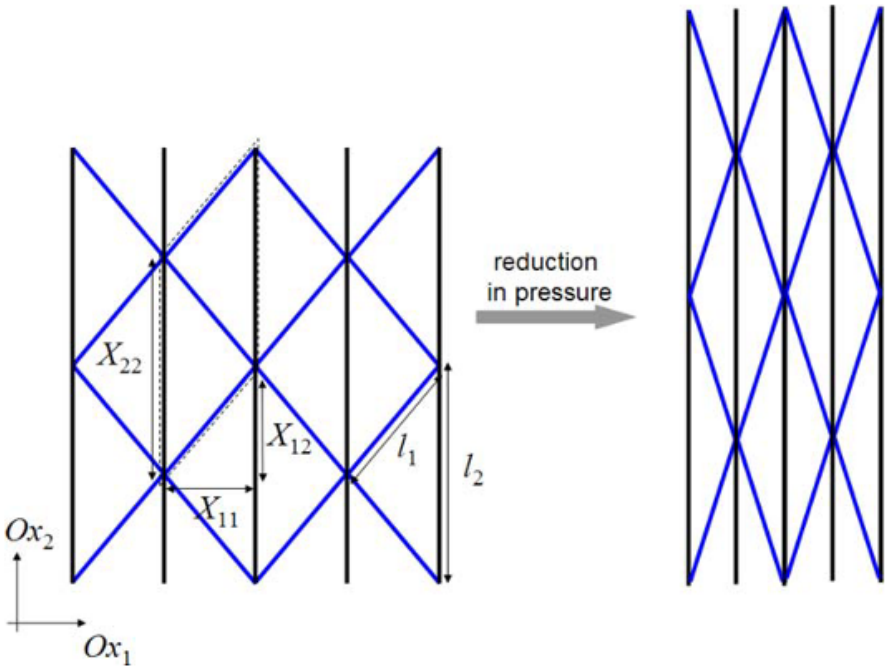

Figure 2.1: An example of a 2D metamaterial system with NLC (in one direction), made of two base materials [23].

$$\left.\begin{aligned}
\varepsilon_1^1 &= \frac{1}{X_1}\left(\frac{\partial X_1}{\partial \theta}d\theta^1 + \frac{\partial X_1}{\partial \theta_2}d\theta_2^1 + \ldots + \frac{\partial X_1}{\partial \theta_n}d\theta_n^1\right)\\
\varepsilon_2^1 &= \frac{1}{X_2}\left(\frac{\partial X_2}{\partial \theta_1}d\theta_1^1 + \frac{\partial X_2}{\partial \theta_2}d\theta_2^1 + \ldots + \frac{\partial X_2}{\partial \theta_n}d\theta_n^1\right)\\
\varepsilon_3^1 &= \frac{1}{X_3}\left(\frac{\partial X_3}{\partial \theta_1}d\theta_1^1 + \frac{\partial X_3}{\partial \theta_2}d\theta_2^1 + \ldots + \frac{\partial X_3}{\partial \theta_n}d\theta_n^1\right)\\
\varepsilon_1^2 &= \frac{1}{X_1}\left(\frac{\partial X_1}{\partial \theta_1}d\theta_1^2 + \frac{\partial X_1}{\partial \theta_2}d\theta_2^2 + \ldots + \frac{\partial X_1}{\partial \theta_n}d\theta_n^2\right)\\
\varepsilon_2^2 &= \frac{1}{X_2}\left(\frac{\partial X_2}{\partial \theta_1}d\theta_1^2 + \frac{\partial X_2}{\partial \theta_2}d\theta_2^2 + \ldots + \frac{\partial X_2}{\partial \theta_n}d\theta_n^2\right)\\
\varepsilon_3^2 &= \frac{1}{X_3}\left(\frac{\partial X_3}{\partial \theta_1}d\theta_1^2 + \frac{\partial X_3}{\partial \theta_2}d\theta_2^2 + \ldots + \frac{\partial X_3}{\partial \theta_n}d\theta_n^2\right)\\
\varepsilon_1^3 &= \frac{1}{X_1}\left(\frac{\partial X_1}{\partial \theta_1}d\theta_1^3 + \frac{\partial X_1}{\partial \theta_2}d\theta_2^3 + \ldots + \frac{\partial X_1}{\partial \theta_n}d\theta_n^3\right)\\
\varepsilon_2^3 &= \frac{1}{X_2}\left(\frac{\partial X_2}{\partial \theta_1}d\theta_1^3 + \frac{\partial X_2}{\partial \theta_2}d\theta_2^3 + \ldots + \frac{\partial X_2}{\partial \theta_n}d\theta_n^3\right)\\
\varepsilon_3^3 &= \frac{1}{X_3}\left(\frac{\partial X_3}{\partial \theta_1}d\theta_1^3 + \frac{\partial X_3}{\partial \theta_2}d\theta_2^3 + \ldots + \frac{\partial X_3}{\partial \theta_n}d\theta_n^3\right)
\end{aligned}\right\}. \tag{2.5}$$

The Greek letter ε denotes the different strains induced in the direction denoted by the subscript due to a load in the direction denoted by the superscript. The strains are a function of the unit cell dimension X and the inclination angles θ. Finally, n denotes the total number of ribs.

Fig. 2.2 describes an example of a 2D system exhibiting NLC as a result of rib rotation. This system displays NLC behavior in one of the two orthogonal directions when the external pressure is reduced. This system is porous and allows fluid to pass through the system. The system in the figure experiences NLC behavior in the Ox_2 direction but positive linear compressibility in the Ox_1 direction.

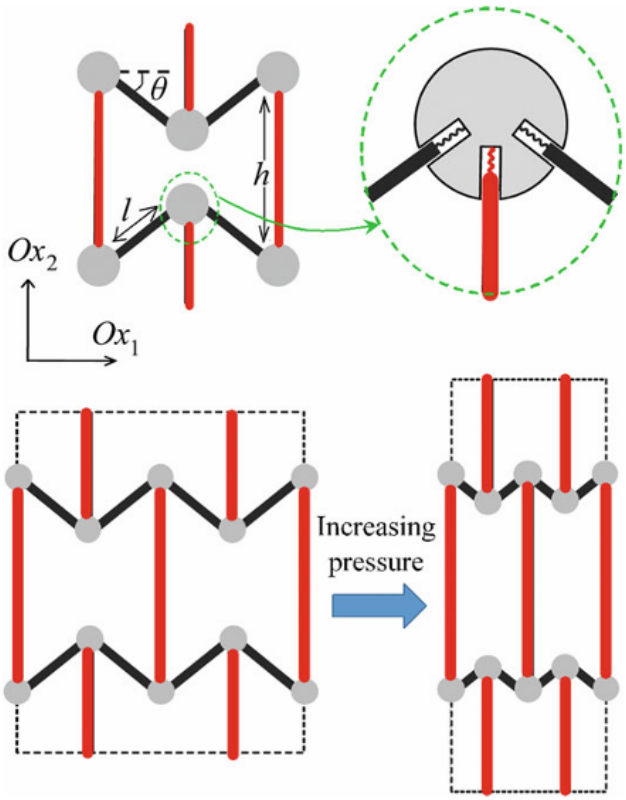

Figure 2.2: An example of an NC system with a rotational constraint exhibiting NLC [13, 26].

Combined Mode

The combined mode of cellular NC metamaterial system uses a combination of both rib stretching and rotation to achieve its deformation. The strains of these systems are a function of both the rib length and the inclination angles. The equation of strains is merely an addition from both the components in Eq.2.4 and Eq.2.5. A couple of porous 2D metamaterial systems that exhibit NLC behavior are shown in Fig. 2.3.

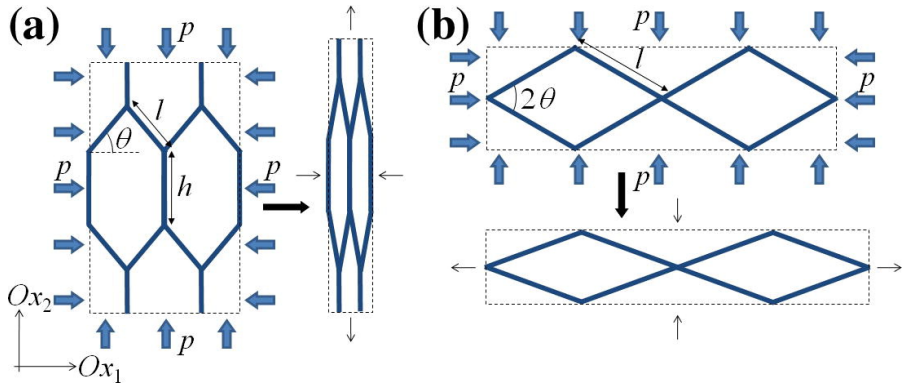

Figure 2.3: Schematics of **(a)** a hexagonal honeycomb and **(b)** a wine-rack model undergoing deformation due to increasing external pressure [24]. The hexagonal honeycomb model only exhibits NLC behavior in the Ox_2 direction while the wine-rack model only exhibits NLC behavior in the Ox_1 direction.

2.1.2. Bi-material Strip System

The porous bi-material strip system put forward by Gatt and Grima [7], exploits the difference in compressibility values of two materials that are attached together. This difference in compressibility values leads to the bending of linkages, which ultimately leads to a change in unit cell dimensions. This is

ilustrated in Fig. 2.4. The resulting system is symmetric and therefore exhibits NLC in both orthogonal directions, along with an overall NAC behavior.

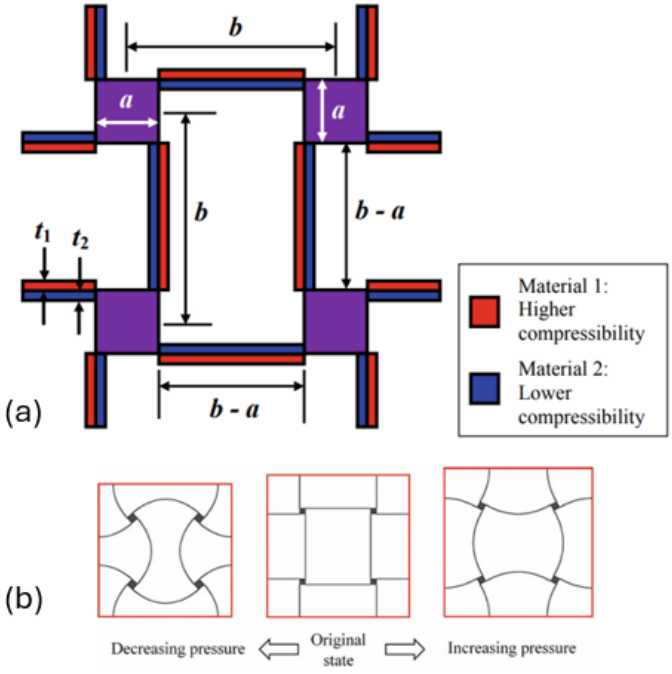

Figure 2.4: Schematic representation of **(a)** a porous bi-material unit cell that exhibits an overall NAC behavior and NLC behavior along the two orthogonal axes and **(b)** the same unit cell deforming under change in pressure [7, 13].

2.1.3. Interconnected Membrane System

Finally, interconnected membrane systems are systems where specific shapes of a particular material are attached together in groups of four (square array) or six (hexagonal array). They take advantage of the fact that when external pressure is applied to these shapes, they tend to decrease in area and form another shape. This change in shape ultimately leads to an increase in the effective area/volume of the unit cell when external pressure is increased, leading to NLC behavior [13]. The metamaterials of interconnected membrane systems are 2D and porous in nature, showing negative area compressibility and equal NLC in the two orthogonal directions. An example of a square array interconnected membrane system made up of octagonal shapes is illustrated in Fig. 2.5. Under an increase in external pressure, the octagonal shapes deform towards a more square shape which ultimately leads to overall unit cell showing NAC and NLC behavior.

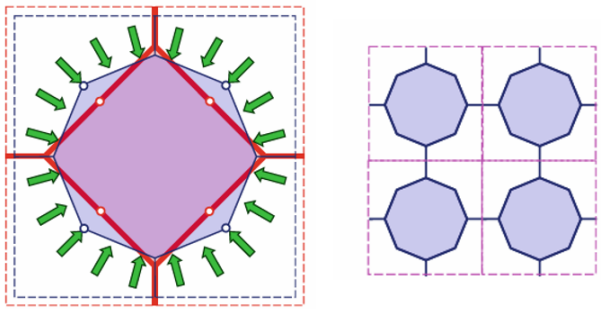

Figure 2.5: Schematic representation of an interconnected membrane system unit cell that consists of a material (shaded blue) in the shape of an octagon that under pressure deforms to a more square shape leading to negative area compressibility (left). The square array is made up of four such cells (right) [13].

2.2. 3D Isotropic Negative Linear Compressibility Metamaterials

Qu et al. [33] proposed a 3D metamaterial design that is isotropic and exhibits NLC. Each unit cell consists of eight hollow crosses connected to each other with thin lever arms. The warping of the thin membranes in the hollow crosses leads to the rotation of the thin lever arms. This ultimately leads to an overall decrease in volume when external pressure is increased and vice versa. This is illustrated in Fig.2.6.

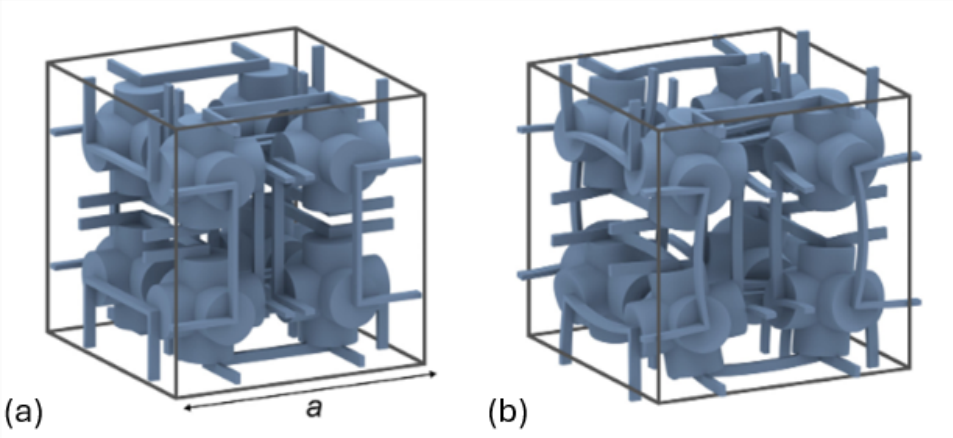

Figure 2.6: (a) Unit cell of the 3D metamaterial design proposed by Qu et al. made up of 8 hollow crosses. **(b)** The same unit cell expanding in volume under applied external pressure [33]. a is the unit cell side length.

Qu et al. [8] further improved this design to achieve a linear compressibility of -4.7%/bar under pressure control. This value is six times larger than the compressibility obtained in the initial design shown in Fig. 2.6. Each unit cell consists of one hollow cube with four connectors attached on each face. Similar to the initial design, the deformation of the inner cube rotates the four connectors attached to it which ultimately leads to a change in length of the overall unit cell. This is illustrated in Fig.2.7.

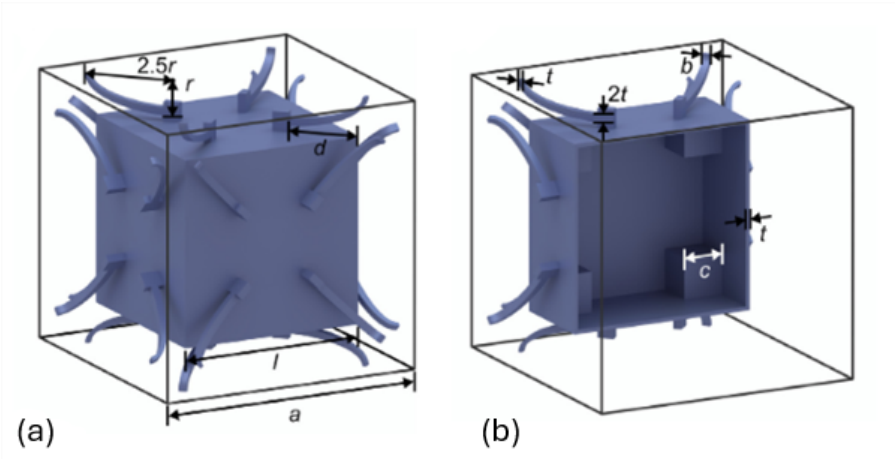

Figure 2.7: (a) Improved unit cell of the 3D metamaterial design proposed by Qu et al. **(b)** Cross-section of the unit cell that shows the internal design (right) [8]. a,l,d,r,c,b and t are dkmensional design parameters of the unit cell.

2.3. Metamaterial Design using Topology Optimization

Two methods are identified for the design of a mechanical metamaterial using TO. The first method is through the inverse homogenization method and the second one is by a CM design formulation. These two methods are desribed in Fig. 2.8.

In the homogenization method, a base cell that forms the repetitive unit of a periodic material is used to derive the effective properties of the periodic material through a number of FE analysis test cases. However, in the inverse homogenization method, the desired material properties are first defined and an

optimal material layout (for the base cell) satisfying those properties is then derived through a number of FE analysis tests. This method has been used and proven to deliver mechanical metamaterials, particularly NPR metamaterials [34].

Metamaterials can also be designed through a CM formulation, where every unit cell is a CM [35, 36]. These CMs can be designed using TO [37, 38, 39]. This CM forms the basis of the metamaterial (base cell) and the macroscopic properties of the material can be defined based on the output displacement of the CM given a certain input displacement/load.

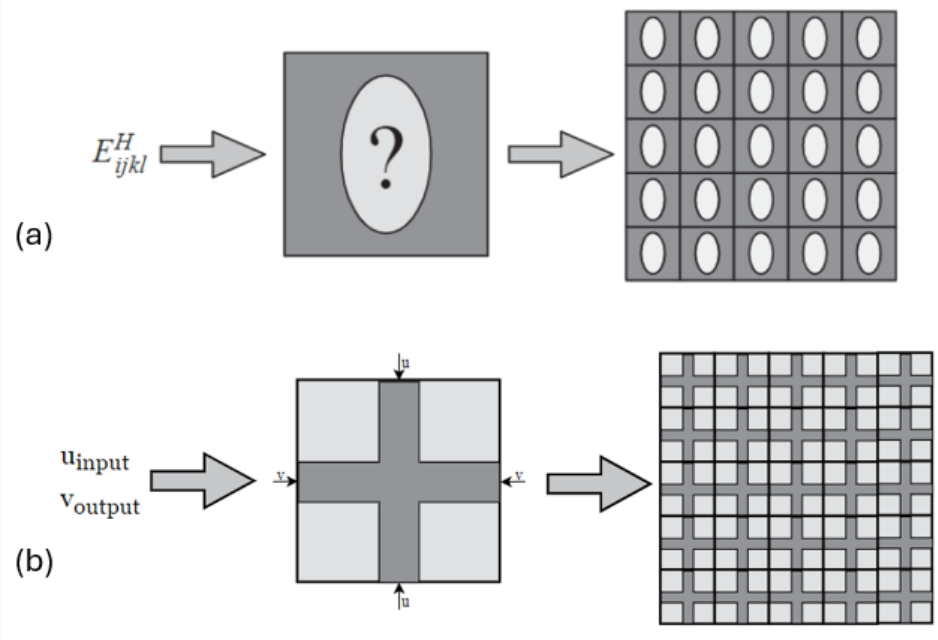

Figure 2.8: (a) The inverse homogenization design process outputs a material (right) that fulfills the required material properties E^H_{ijkl} by designing the optimal micro-structural topology (center) [34]. **(b)** The CM formulation outputs the required material layout (right) by designing the optimal CM (center) that forms the base cell of this material. The CM design is decided by the input load/displacement **u** and the output displacement **v**.

2.3.1. Inverse Homegenization

Developed from the homogenization method, which involved taking a small repetitive unit (base cell) consisting of one or more materials and running a number of FE analysis tests on it to derive the properties of the unit cell, inverse homogenization involves defining the value of these properties and then finding the material distribution of each unit cell that would contribute to those overall properties. Sigmund [40] laid out a blueprint for the design of metamaterials through the inverse homogenization method and formulated the optimization problem as follows:

$$\left.\begin{aligned} \min_{\boldsymbol{\rho}} \quad & : \Phi(C^*_{ijkl}(\boldsymbol{\rho})) \\ \text{s.t.} \quad & : \sum_{e=1}^{N} v^e \rho^e / V_0 \leq f \\ & : g_i(C^*_{ijkl}(\boldsymbol{\rho})) \leq g^*_i, \qquad i = 1, \cdots, M \\ & : \mathbf{K}(\boldsymbol{\rho})\mathbf{u}_i = \mathbf{F}_i, \qquad i = 1, \cdots, m \\ & : 0 \leq \boldsymbol{\rho} \leq 1 \end{aligned}\right\}, \tag{2.6}$$

where $\Phi(C^*_{ijkl}(\boldsymbol{\rho}))$ is the function of the homogenized material that needs to be minimized; v^e, ρ^e, V_0 and f are the elemental volume, elemental density, total design space volume and chosen volume fraction, respectively; $g_i(C^*_{ijkl}(\boldsymbol{\rho}))$ are the constraints and g^*_i are the limiting values of those constraints that are chosen. $\mathbf{K}(\boldsymbol{\rho})\mathbf{u}_i = \mathbf{F}_i$ is the linear FE equation used to calculate the homogenized property

values of the unit cell. Finally, M, m and N denote the total number of constraints, test loads and elements, respectively.

Larsen et al. [41] used inverse homegenization to find metamaterial structures with negative Poisson's ratios, through a least-squares optimization problem where the objective function was defined as:

$$\text{min} \quad : \Phi = (\boldsymbol{E}^H_{ijkl} - \boldsymbol{E}^*_{ijkl})^2. \tag{2.7}$$

$\boldsymbol{E}^H_{ijkl}$ is the desired elasticity tensor of the unit cell and $\boldsymbol{E}^*_{ijkl}$ is the elasticity of the unit cell after optimization. This value is obtained through homogenization process which solves a FE problem of the design to obtain the property values. This is further illustrated in Fig.2.9.

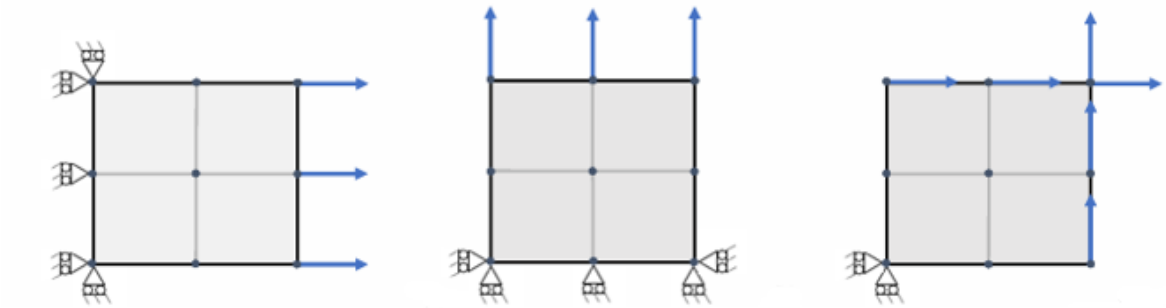

Figure 2.9: A discretized base cell with two by two elements.Test unit strains are applied to corner nodes in three FE cases as ε = {1 0 0} (left), ε = {0 1 0} (center) and ε = {0 0 1} (right).

2.3.2. Compliant Mechanism Formulation

CM synthesis using TO can be a viable method of metamaterial design, specifically for metamaterial properties that involve displacements, such as NPR and NLC metamaterials. As illustrated in Fig 2.10, these metamaterial can be designed using CM synthesis because these properties are a result of a distinct input load that results in a distinct displacement, both of which can be easily defined for the CM synthesis problem.

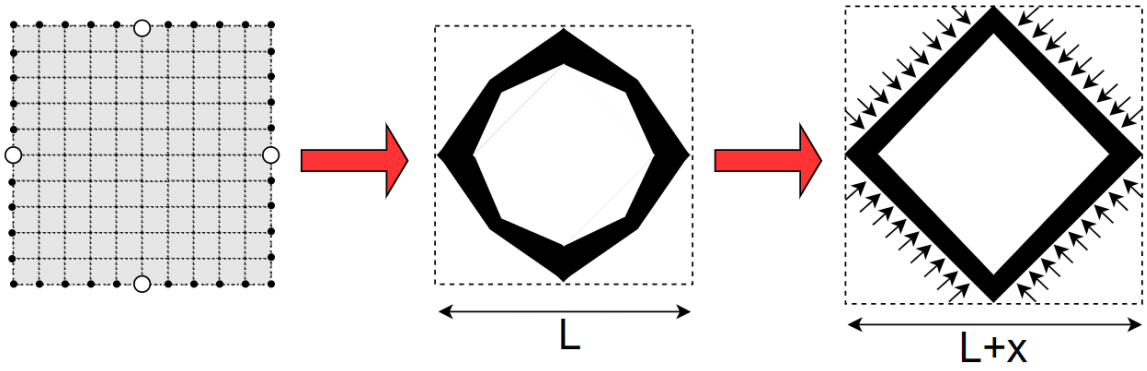

Figure 2.10: Example of a possible 2D NLC metamaterial design using the CM formulation. Initial material space (left) along with the required initial load points (black dots) and desired displacement points (white dots). Optimized CM (center) that forms the base cell. Base cell deformed under load, pressure load in this case (right). The required displacement/change in length can be observed as the side length L increases to L+x.

The foundation of CM synthesis using TO was first put forward by Ananthasuresh et al. [37], Sigmund [38], and Ananthasuresh et al. [39]. This led to two main approaches: one put forward by Sigmund [42], where the output load was defined as a spring force, and the second put forward by Frecker et al. [43], which is a multi-criteria approach based on two mutual energies. The two methods are illustrated in Fig. 2.11.

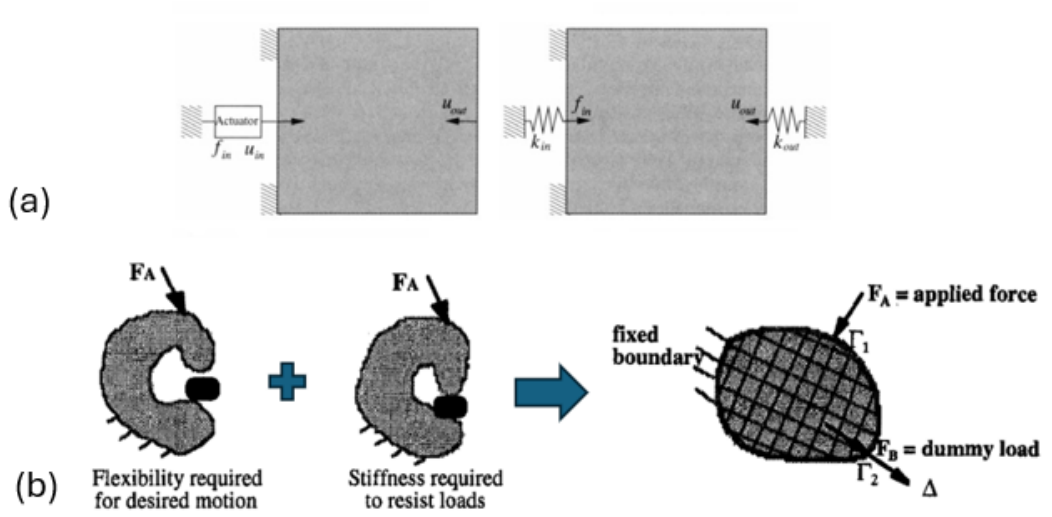

Figure 2.11: (a) First approach where the output load is defined as a spring force [18]. **(b)** Second approach where the optimization criteria not only depends on the flexibility of the mechanism but also on its stiffness [43].

2.4. Density-based Topology Optimization for Pressure Loads

TO for NLC metamaterials involve the application of pressure loads. These loads pose an added difficulty, as they are design-dependent and have a changing load boundary. This means that the direction and location of the loads depends on the shape and topology of the design. This problem was first addressed by Hammer and Olhoff [44], who tackled this through the use of iso-density curves and surfaces to determine the application curve or surface of the pressure load. However, boundary identification proved to be cumbersome and challenging. The steps followed by this design method are illustrated in Fig. 2.12. Some of these problems were mitigated in subsequent research works [45, 46, 47, 48, 49]. These boundary identification methods also failed to account for pressure load sensitivities. These load sensitivities strongly contribute towards finding the most optimal pressure-actuated CM (PaCM). Therefore, it is important to find an inexpensive way to calculate them.

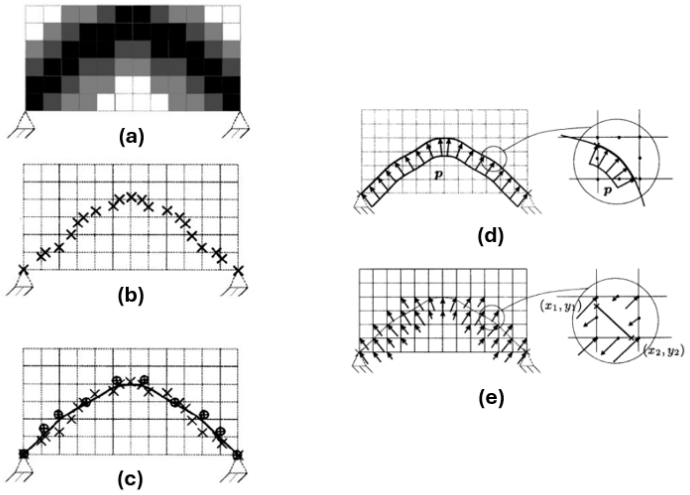

Figure 2.12: The parameterization of a load bearing surface based on **(a)** a non-uniform and discontinuous density distribution. **(b)** Identified equal density points.**(c)** The Bézier curve that fits these points. **(d)** Identified pressure loading curve and pressure distribution. **(e)** The curve crossing through an element is approximated as a line passing through it and the intersection points (x_1, y_1, x_2, y_2) help determine the consistent nodal forces acting on the element [44].

Another school of thought [50, 51, 52, 53, 54, 55] emerged that sought to steer clear of boundary identification methods completely, using physical fields or phases. The load boundaries are implicitly obtained through the formulation in these methods. For example, Sigmund and Clausen [50] put forward a mixed formulation approach which didn't require surface load parametrizations. In this method, the standard FE displacement formulations is replaced with a mixed form that includes pressure as another separate variable. A "void" phase is also defined, that acts as a hydrostatic incompressible fluid, allowing for the transfer of pressure forces through it. Finally, to prevent the optimizer from exploiting this incompressibility, another phase called "fluid" phase is introduced. This leads to a three-phase TO method. While these methods were able to skip the cumbersome boundary identification step, they didn't take into account load sensitivities.

To tackle this issue, Kumar et al. [56] proposed a method that utilizes Darcy's Law to implicitly identify the pressure boundary. This is realized through the clever use of a drainage term, wherein only the surfaces in contact with the pressure experience the pressure load. This method also allows for the analytical calculation of the load sensitivities with respect to the design variables through the adjoint-variable method. This method is used to find the optimal PaCMs [57], which makes it a great tool to design the unit cells of NLC metamaterials. Fig. 2.13 graphically represents the steps taken to calculate the consistent nodal forces resulting from the pressure applied and Fig. 2.14, illustrates a design-dependent problem that utilizes Darcy's Law to find the changing pressure boundary.

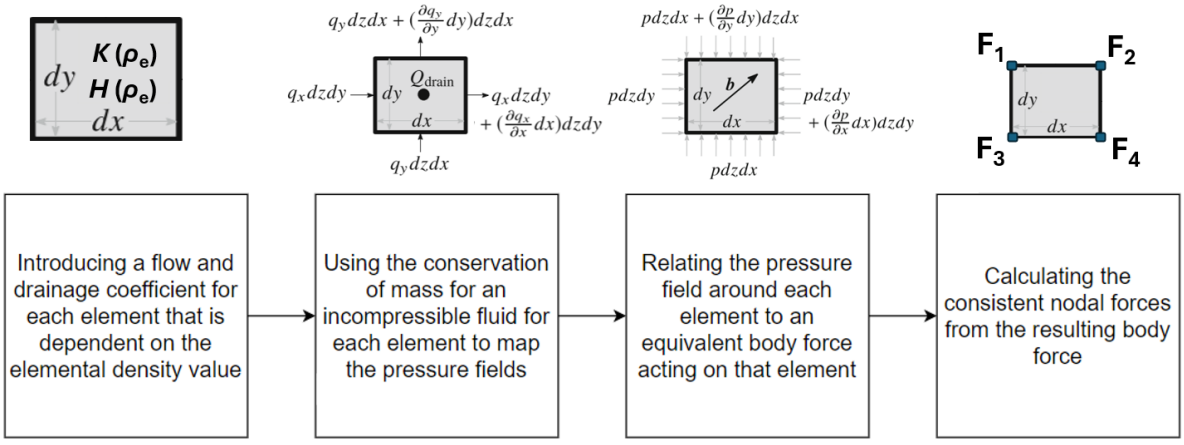

Figure 2.13: Graphical representation of the steps taken to calculate the consistent nodal forces resulting from the pressure applied. Where dx, dy, $K(\rho_e)$, $H(\rho_e)$, q, Q_{drain}, p, b, and F are the element's dimension in x, dimension in y, flow coefficient, drainage coefficient, flux flowing through it, volumetric drainage per second, pressure applied, equivalent body force experienced, consistent nodal forces experienced, respectively [56].

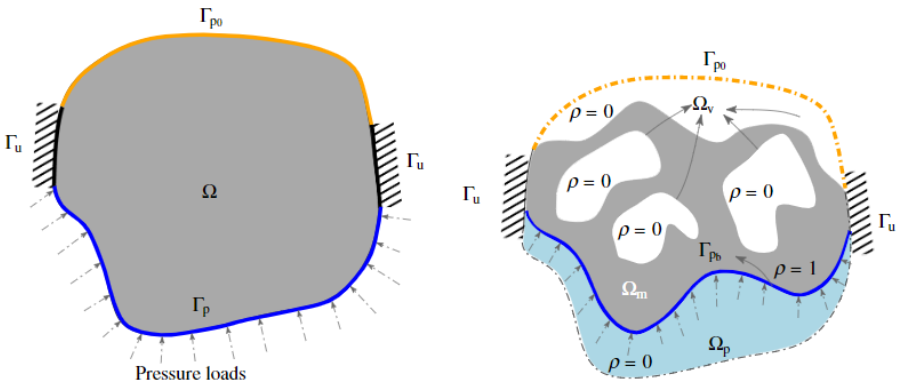

Figure 2.14: Evolution of the pressure boundaries (initial input Γ_p, output Γ_{p_0} and evolving Γ_{p_b}) in a design optimization problem that utilizes Darcy's Law to map the pressure field and the evolving pressure boundary, where Ω and Ω_m indicate the design domain and the solid region respectively. Ω_p and Ω_v indicate the pressurized and pressurized void regions respectively. Finally, Γ_u and ρ indicate the fixed displacement boundary and the material density, respectively[56].

2.5. Design Method

Based on the state of the art, there are numerous options available when selecting the most appropriate design methodology for NLC metamaterials.

1. Type of mechanism: From section 1.4 it is clear that CMs possess several advantages that make them better suited for the design of NLC metamaterials, as compared to rigid body mechanisms.
2. CM synthesis method: Structural optimization is the best CM synthesis method when it comes to engineering NLC metamaterials because it not only fulfills many requirements that are desired when it comes to designing NLC metamaterials, but also provides additional advantages over other CM synthesis methods. These reasons are elucidated in section 1.4.
3. Method of optimization: There are different methods that can be used for structural optimization. However, the versatility of density-based TO to solve a large variety of problems, coupled with the extensive literature on different topics, make it one of the easiest implementable methods.
4. Metamaterial design method: As mentioned in section 2.3, there are two main methods of tackling a metamaterial design problem using density-based TO. Based on the task of NLC metamaterial design, the CM formulation seems to be the better method as the inverse homegenization method doesn't have any flexibility for the implementation of design-dependent loads. It is also quite restrictive as compared to a CM formulation.[1]
5. Application of pressure load: The "Darcy's Method" of pressure load application put forward by Kumar et al. [56] is better suited for metamaterial design using the CM formulation. This is because the "Darcy Method"[2] takes pressure load sensitivities into account which leads to better optimized CM results [56, 58].

These are the reasons why this report will tackle the problem of NLC metamaterial design by designing the metamaterial unit cell as a PaCM that will be designed using density-based TO. Finally, the pressure loads in this problem will be applied using the "Darcy Method" put forward by Kumar et al. [56].

1 In the CM formulation, we can choose the location and number of output points.
2 The pressure force application method put forward by Kumar et al. [56] that uses Darcy's Law to map the pressure field is hereby referred to as "Darcy Method".

3

Methodology

3.1. Design Method

For the design of an NLC unit cell, the density-based TO formulation was used and the modified SIMP approach was employed to relate the elemental stiffness matrix of its design variable as shown in Eq. 1.2. The optimization problem of a density-based TO formulation can be written as:

$$\left.\begin{aligned} \min_{\boldsymbol{\rho}} \quad & : \Phi(\boldsymbol{\rho}) \\ \text{s.t.} \quad & : \mathbf{A}_i(\boldsymbol{\rho})\mathbf{x}_i = \mathbf{B}_i, \qquad i = 1, \cdots, M \\ & : f_i(\boldsymbol{\rho}) = f_i^*, \qquad i = 1, \cdots, N \\ & : g_i(\boldsymbol{\rho}) \leq g_i^*, \qquad i = 1, \cdots, L \\ & : 0 \leq \boldsymbol{\rho} \leq 1 \end{aligned}\right\}, \tag{3.1}$$

where linear set of equations $\mathbf{A}_i(\boldsymbol{\rho})\mathbf{x}_i = \mathbf{B}_i$ are the different state equations that are used to calculate the state variables. Functions $f_i(\boldsymbol{\rho})$ are limited by f_i^* and are also called equality constraints, functions $g_i(\boldsymbol{\rho})$ are limited by g_i^* and are called inequality constraints. M, N and L signify the number of state equations, equality constraints and inequality constraints, respectively.

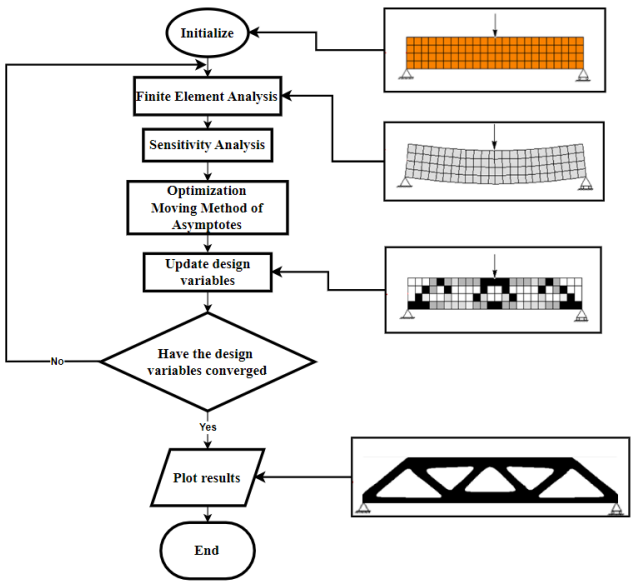

Figure 3.1: Flowchart of density-based TO method using method of moving asymptotes.

The optimization process begins by initializing a density layout. The objective function relating to that density layout is calculated using the related state equations. The density layout is updated based on an optimization scheme. The optimization scheme used for this problem is the method of moving asymptotes (MMA). This method introduced by Svanberg [59] is preferred for its computation speed and versatility in handling multi-constraint problems. The optimization scheme uses design sensitivities that are based on the objective, state and constraint equations to change the density layout towards an optimized layout. This iteration process continues until an optimized density layout is obtained. Lastly, other regularization tools and techniques like filtering, passive elements, and symmetric sensitivity averaging can be used to obtain desirable results based on the design problem and errors faced [18]. The process can be visualized in Fig. 3.1.

3.1.1. Design Space

For a 2D and 3D NLC metamaterial unit cell design, the design space is modeled as a square and cubic domain that is discretized into equal number of square and cubic elements in all two and three orthogonal directions, respectively. This helps obtain symmetric designs with isotropic material properties. The domain in the 2D and 3D case represents one-fourth and one-eighth of the total metamaterial unit cell, respectively. This is shown in Fig. 3.2.

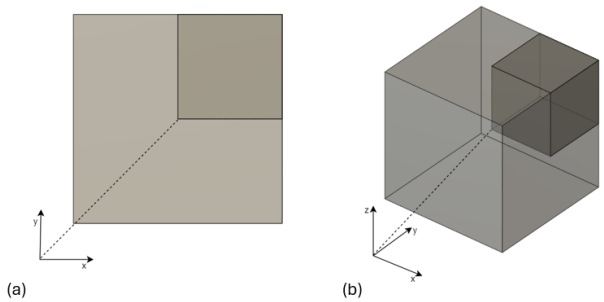

Figure 3.2: (a) Design space (dark gray) and overall 2D unit cell (light gray). **(b)**Design space (dark gray) and overall 3D unit cell (light gray).

Each element consists of eight nodes and every node is associated to three displacement and one pressure degrees of freedom. Every element is associated to a particular density value that is updated after every iteration, until an optimized value is obtained. The global nomenclature of the elements and nodes and the local nomenclature of an element's associated degrees of freedom and density is illustrated in Fig. 3.3. For the 2D case one can refer to [60].

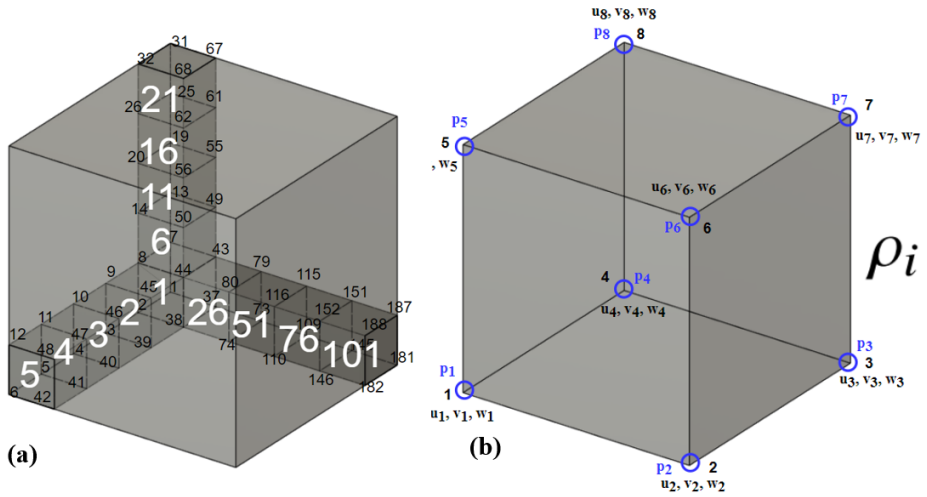

Figure 3.3: (a) Mesh grid nomenclature: Global format. Illustrating the element numbers (white) and their node numbers (black). **(b)** Nomenclature for element i: Local format. Illustrating the nodes; their displacement degrees of freedom in their three orthogonal directions (u, v and w); and pressure degrees of freedom (p). ρ_i represents the design variable of element i.

3.1.2. Objective Function

As discussed in Section 2.5, the NLC metamaterial design is generated using a CM formulation. A flexibility-stiffness based multi-criteria formulation developed by Saxena and Ananthasuresh [61] and Frecker et al. [43] is implemented in this case. This can ensure that the obtained CM is not only stiff enough to handle the actuating loads, but can also provide the desired deformation. The function driving the stiffness is the strain energy (SE) or compliance, which is minimized, whereas the function that is driving the output deformation is the mutual strain energy (MSE). The objective function can therefore be written as [61]:

$$\Phi(\mathbf{u}, \mathbf{v}, \boldsymbol{\rho}) = -\frac{MSE(\mathbf{u}, \mathbf{v}, \boldsymbol{\rho})}{2SE(\mathbf{u}, \boldsymbol{\rho})} = -\frac{\mathbf{v}^{\mathsf{T}}\mathbf{K}\mathbf{u}}{\mathbf{u}^{\mathsf{T}}\mathbf{K}\mathbf{u}}, \tag{3.2}$$

where **u**, **v**, and **K** are the global displacement vector, output deformation vector and the global stiffness matrix, respectively. It is important to note that in this CM formulation an output stiffness k_{ss} is added at the output location, which represents the work piece stiffness.

3.1.3. State Equations

State equations help us find the required state variable given a certain value of the design variable, which in turn is required to calculate the objective function. As seen in Eq. 3.2, the state variables that influence the CM objective function are **u** and **v**. The first state equation is straightforward and comes from the CM formulation put forward by Saxena and Ananthasuresh [61].

$$\sum_{e=1}^{N} E_e(\rho_e)\mathbf{k}_e\mathbf{v}_e = \mathbf{K}\mathbf{v} = \mathbf{F}_{\mathsf{d}}, \tag{3.3}$$

where $E_e(\rho_e)$ is the density-dependent elemental Young's modulus as shown in Eq. 1.2. $\mathbf{k}_e$ and $\mathbf{v}_e$ are the elemental stiffness matrix and elemental output deformation vector. N denotes the total number of elements in the design space and $\mathbf{F}_{\mathsf{d}}$ is a unit dummy force vector that is in the same direction as that of the output deformation.

The second state equation can be found through the FE equation relating the global displacement vector to the global force vector.

$$\sum_{e=1}^{N} E_e(\rho_e)\mathbf{k}_e\mathbf{u}_e = \mathbf{K}\mathbf{u} = \mathbf{F}, \tag{3.4}$$

where $\mathbf{u}_e$ is the elemental displacement vector and **F** is the global force vector. While the calculation of the global stiffness matrix **K** is straightforward, the global force vector **F** is constantly changing and isn't easy to calculate. Additional state equations are required to firstly map the pressure points and secondly to relate the pressure points to nodal forces. This can be done using the "Darcy Method".

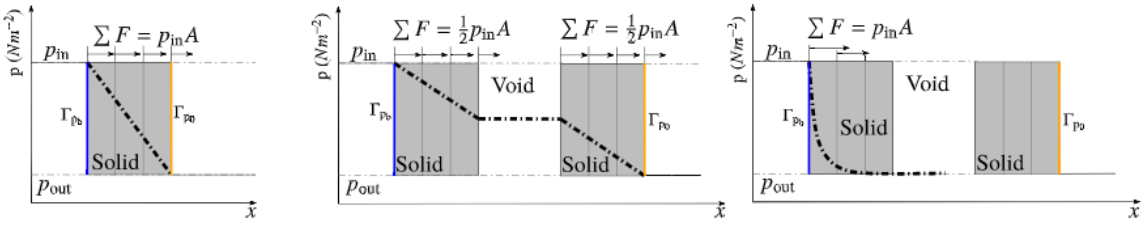

(a) pressure drop over a single boundary without drainage term

(b) pressure drop over two boundaries without drainage term

(c) pressure drop over two boundaries with drainage term

Figure 3.4: Behavior of a 1D pressure field (thick dash-dotted lines/curves) when using Darcy's law on a porous material of three elements. **(a)** p_{in}, p_{out}, $\sum F$ and A are the input pressure, output pressure, total force on the boundary and cross-section sectional area, respectively [56]. To visualize these cases, one may refer to [60].

Darcy's Law defines the ability of a fluid to flow through porous media, such as rock, soil, or sandstone. It states that the fluid flow through a unit area is directly proportional to the pressure drop per unit length and inversely proportional to the resistance of the porous medium to the flow [62].

$$\boldsymbol{q} = -\frac{\kappa}{\mu}\nabla p = -K(\rho_e)\nabla p, \tag{3.5}$$

where $\boldsymbol{q}$, κ, μ, and ∇p represent the flux (ms^{-1}), permeability (ms^2), fluid viscosity ($Nm^{-2}s$) and pressure gradient (Nm^{-3}), respectively. Further, K ($m^4N^{-1}s^{-1}$) is termed herein as a flow coefficient which expresses the ability of a fluid to flow through a porous medium. The flow coefficient of each element is related to its density ρ_e. This equation not only allows to map the pressure field over the design space but is also a function of the design variable (ρ_e). $K(\rho_e)$ is modelled using a smooth Heaviside function [56] as:

$$K(\rho_e) = k_\mathsf{v} - k_\mathsf{vs}\frac{\tanh(\beta_\mathsf{k}\eta_\mathsf{k}) + \tanh(\beta_\mathsf{k}(\rho_e - \eta_\mathsf{k}))}{\tanh(\beta_\mathsf{k}\eta_\mathsf{k}) + \tanh(\beta_\mathsf{k}(1 - \eta_\mathsf{k}))}, \tag{3.6}$$

where $k_\mathsf{vs} = (k_\mathsf{v} - k_\mathsf{s})$ and k_v and k_s are the flow coefficients for void ($\rho_e = 0$) and solid ($\rho_e = 1$) elements, respectively. The value of η_k and β_k are adjustable parameters that control the position of the step and slope of the Heaviside function. The flow coefficient $k_\mathsf{s} << k_\mathsf{v}$, resulting in a greater drop in pressure when passing through a solid elements, as the value of $K(\rho_e) = k_\mathsf{s}$ in a solid element ($\rho_e = 1$), and $K(\rho_e) = k_\mathsf{v}$ in a void element ($\rho_e = 0$).

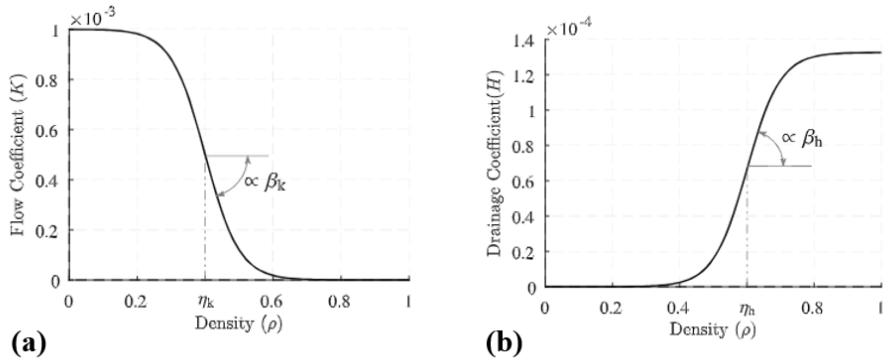

Figure 3.5: (a) A Heaviside function used to represent the density-dependent flow coefficient $K(\rho_e)$. For the plot, η_k = 0.4 and β_k = 10 have been used. It can be observed that when $\eta_\mathsf{k} > \rho_e$, $K(\rho_e) = k_\mathsf{v}$ and when $\eta_\mathsf{k} < \rho_e$, $K(\rho_e) = k_\mathsf{s}$. **(b)** A Heaviside function used to represent the drainage coefficient $H(\rho_e)$ using the Heaviside parameters η_k = 0.6 and β_k = 10. Herein, r = 0.1, Δs = 2 mm and k_d = $10^{-10}m^4N^{-1}s^{-1}$ are considered to find h_s in Eq. 3.9, which is used for evaluating $H(\rho_e)$ in Eq. 3.8. It can be seen that when $\eta_\mathsf{h} > \rho_e$, $H(\rho_e) \to 0$ and when $\eta_\mathsf{h} < \rho_e$, $H(\rho_e) \to h_\mathsf{s}$ [56].

However, pressure fields mapped through this equation alone lead to a more gradual drop in pressure. This leads to forces (due to pressure) being applied on the internal walls. These walls are not in contact with the pressurized fluid and should not experience any force acting on them. As depicted in Fig. 3.4, there should be a sudden drop in pressure over the first solid boundary and this can be achieved by coupling the Darcy's Law equation with an additional drainage term [56]. This can be mathematically written as:

$$Q_\mathsf{drain} = -H(\rho_e)(p - p_\mathsf{out}), \tag{3.7}$$

where Q_drain denotes volumetric drainage per second in a unit volume (s^{-1}). H, p, p_out are the drainage coefficient ($m^2N^{-1}s^{-1}$), the continuous pressure field (Nm^{-2}), and the external pressure (Nm^{-2}), respectively. H is modeled as a smooth Heaviside function [56] that is dependent on the elemental density:

$$H(\rho_e) = h_{\mathsf{s}} \frac{\tanh(\beta_{\mathsf{h}}\eta_{\mathsf{h}}) + \tanh(\beta_{\mathsf{h}}(\rho_e - \eta_{\mathsf{h}}))}{\tanh(\beta_{\mathsf{h}}\eta_{\mathsf{h}}) + \tanh(\beta_{\mathsf{h}}(1 - \eta_{\mathsf{h}}))}. \tag{3.8}$$

Similar to β_{k} and η_{k}, β_{h} and η_{h} are adjustable parameters. The drainage coefficient of solid h_{s} is used to control the thickness of the pressure-penetration layer. It is related to k_{s} as:

$$h_{\mathsf{s}} = \left(\frac{\ln r}{\Delta s}\right)^2 k_{\mathsf{s}}, \tag{3.9}$$

where r is the ratio of input pressure (p_{in}) at depth Δs, i.e., $p|_{\Delta s} = r p_{\mathsf{in}}$. Furthermore, Δs is the penetration depth of pressure, which can be set to the width or height of few elements [56].

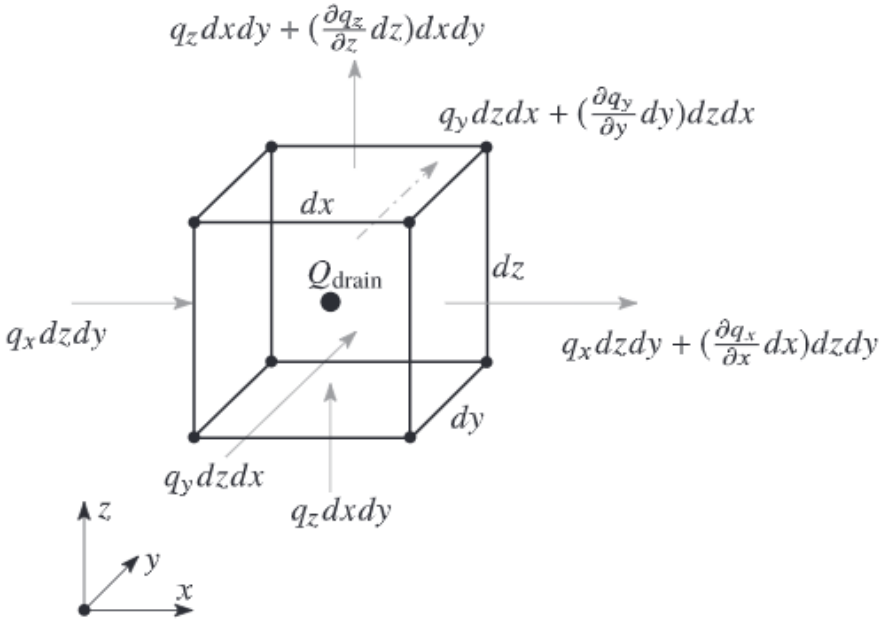

Figure 3.6: A schematic diagram for in- and outflow through an infinitesimal element with volume $\mathrm{d}V = \mathrm{d}x\mathrm{d}y\mathrm{d}z$. Q_{drain} is the volumetric drainage term [63].

The pressure field can be calculated through the state equilibrium equation for the incompressible fluid flow through an element. This is visualised in Fig. 3.6 and is written as [63]:

$$\nabla \cdot \boldsymbol{q} - Q_{\mathsf{drain}} = 0. \tag{3.10}$$

The weak form of Eq. 3.10 within an element e gives:

$$\underbrace{\int_{\Omega_e} \left(K\mathbf{B}_{\mathsf{p}}^{\mathsf{T}}\mathbf{B}_{\mathsf{p}} + H\mathbf{N}_{\mathsf{p}}^{\mathsf{T}}\mathbf{N}_{\mathsf{p}}\right) d\Omega_e}_{\mathbf{A}_e} \mathbf{p}_e = \underbrace{\int_{\Omega_e} H\mathbf{N}_{\mathsf{p}}^{\mathsf{T}} p_{\mathsf{out}}\, d\Omega_e - \int_{\Gamma_e} \mathbf{N}_{\mathsf{p}}^{\mathsf{T}} q_\Gamma \cdot \mathbf{n}_e\, d\Gamma_e}_{\mathbf{f}_e}, \tag{3.11}$$

where $\mathbf{N}_{\mathsf{p}} = [N_1, N_2, N_3, \ldots, N_8]$ are the shape functions for the trilinear hexahedral elements and $\mathbf{p}_e = [p_1, p_2, p_3, \ldots, p_8]^{\mathsf{T}}$ is the elemental nodal pressure vector. The function is integrated over a volume element Ω_e. The matrix $\mathbf{B}_p$ is equal to the gradient of the shape functions $\mathbf{N}_{\mathsf{p}}$ and $\mathbf{n}_e$ is the boundary normal on surface Γ_e that has a flux of q_Γ passing through it. Globally, this leads to the third state equation,

$$\mathbf{Ap} = \mathbf{f}, \tag{3.12}$$

where **A** is the global flow matrix, **p** and **f** are the global pressure and loading vectors, respectively. When $p_{\text{out}} = 0$ and $q_\Gamma = 0$, the right hand side of the equation equals to zero and the state equation can be rewritten as $\mathbf{Ap} = 0$ [63].

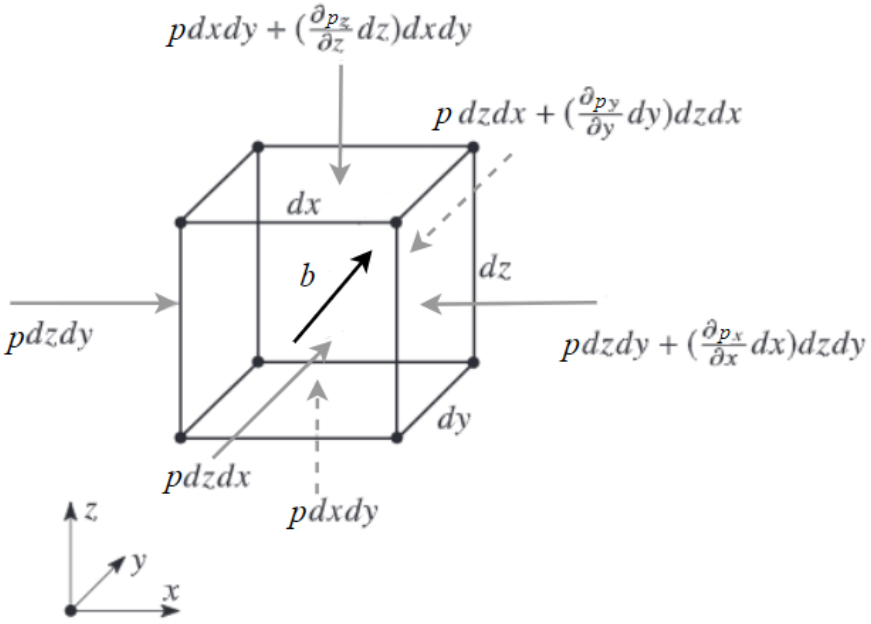

Figure 3.7: A schematic diagram for the body force vector $\boldsymbol{b}$ of an infinitesimal element with volume $\mathrm{d}V = \mathrm{d}x\mathrm{d}y\mathrm{d}z$. p is the uniform pressure load acting on the area perpendicular to the gray arrows [63].

To relate the pressure field to consistent nodal forces, we can express the force resulting from the pressure field in terms of an equivalent body force, as shown in Fig. 3.7. This is mathematically written as [56]:

$$\boldsymbol{b}dV = -\nabla p dV, \tag{3.13}$$

where $\boldsymbol{b}$ is the body force vector. The elemental nodal forces can be written as:

$$\mathbf{F}_e = -\int_{\Omega_e} \mathbf{N}_\mathbf{u}^\mathsf{T} \nabla p d\Omega_e = -\underbrace{\int_{\Omega_e} \mathbf{N}_\mathbf{u}^\mathsf{T} \mathbf{B}_\mathbf{p} d\Omega_e}_{\mathbf{H}_e} \mathbf{p}_e, \tag{3.14}$$

where $\mathbf{F}_e$ and $\mathbf{H}_e$ are the elemental force and global conversion matrix, respectively. $\mathbf{N}_\mathbf{u}$ = [$N_1\mathbf{I}$, $N_2\mathbf{I}$, $N_3\mathbf{I}$, …, $N_8\mathbf{I}$] with **I** being the identity matrix in coordinate space $\mathbb{R}^3$. Globally, the last state equation relating the pressure field to consistent nodal forces is obtained. Mathematically,

$$\mathbf{F} = -\mathbf{Hp}, \tag{3.15}$$

where the pressure vector **p** is related to the force vector **F** through a global conversion matrix **H**. Eqs. 3.3, 3.5, 3.12, 3.15 are the four state equations that are required to solve the optimization problem. This can further be reduced to three state equations by combining Eqs. 3.5 and 3.15 to obtain:

$$\mathbf{Ku} = -\mathbf{Hp}. \tag{3.16}$$

3.1.4. Constraints

In the density-based TO approach, a volume constraint inequality is applied on the design space [64]. Mathematically,

$$\frac{V(\rho)}{V_0} \leq f, \tag{3.17}$$

where $V(\rho)$ and V_0 are the material volume and design domain volume respectively, and f is the prescribed volume fraction.

3.1.5. Design Sensitivity

For gradient-based optimizers like MMA, design sensitivities of the objective function and constraints need to be calculated. The adjoint-variable method can be employed to calculate the objective function sensitivity. This method uses a performance function $\mathcal{L}$ that is described in terms of the objective function and state equations as:

$$\mathcal{L}(\mathbf{u}, \mathbf{v}, \boldsymbol{\rho}) = \Phi(\mathbf{u}, \mathbf{v}, \boldsymbol{\rho}) + \lambda_1^\mathsf{T}(\mathbf{Ku} + \mathbf{Hp}) + \lambda_2^\mathsf{T}(\mathbf{Ap}) + \lambda_3^\mathsf{T}(\mathbf{Kv} + \mathbf{F_d}), \tag{3.18}$$

where λ_1, λ_2 and λ_3, are the Lagrange multipliers. Mathematically [63],

$$\lambda_1^\mathsf{T} = -\frac{\partial \Phi(\mathbf{u}, \mathbf{v}, \boldsymbol{\rho})}{\partial \mathbf{u}}\mathbf{K}^{-1}, \qquad \lambda_2^\mathsf{T} = -\lambda_1^\mathsf{T}\mathbf{H}\mathbf{A}^{-1}, \qquad \lambda_3^\mathsf{T} = -\frac{\partial \Phi(\mathbf{u}, \mathbf{v}, \boldsymbol{\rho})}{\partial \mathbf{v}}\mathbf{K}^{-1}. \tag{3.19}$$

For the objective function written in Eq. 3.2, the calculated Lagrange multipliers are:

$$\lambda_1^\mathsf{T} = -\left(\frac{\mathbf{v}}{2SE} + \mathbf{u}^\mathsf{T}\frac{MSE}{SE}\right), \qquad \lambda_2^\mathsf{T} = \left(\frac{\mathbf{v}}{2SE} + \mathbf{u}^\mathsf{T}\frac{MSE}{SE}\right)\mathbf{H}\mathbf{A}^{-1}, \qquad \lambda_3^\mathsf{T} = \frac{\mathbf{u}^\mathsf{T}}{2SE}. \tag{3.20}$$

The objective sensitivities can then be written as:

$$\frac{d\Phi}{d\boldsymbol{\rho}} = \frac{\partial \Phi}{\partial \boldsymbol{\rho}} + \lambda_1^\mathsf{T}\frac{\partial \mathbf{K}}{\partial \boldsymbol{\rho}}\mathbf{u} + \lambda_2^\mathsf{T}\frac{\partial \mathbf{A}}{\partial \boldsymbol{\rho}}\mathbf{p} + \lambda_3^\mathsf{T}\frac{\partial \mathbf{K}}{\partial \boldsymbol{\rho}}\mathbf{v}. \tag{3.21}$$

Combining Eq. 3.20 and Eq. 3.21

$$\frac{d\Phi}{d\boldsymbol{\rho}} = \frac{MSE}{(2SE)^2}\left(-\mathbf{u}^\mathsf{T}\frac{\partial \mathbf{K}}{\partial \boldsymbol{\rho}}\mathbf{u}\right) + \frac{1}{2SE}\left(\mathbf{u}^\mathsf{T}\frac{\partial \mathbf{K}}{\partial \boldsymbol{\rho}}\mathbf{v}\right) + \underbrace{\frac{MSE}{2(SE)^2}\left(\mathbf{u}^\mathsf{T}\mathbf{H}\mathbf{A}^{-1}\frac{\partial \mathbf{A}}{\partial \boldsymbol{\rho}}\mathbf{p}\right) - \frac{1}{2SE}\left(\mathbf{v}^\mathsf{T}\mathbf{H}\mathbf{A}^{-1}\frac{\partial \mathbf{A}}{\partial \boldsymbol{\rho}}\mathbf{p}\right)}_{\text{Load sensitivities}}. \tag{3.22}$$

Load sensitivities depend on the pressure load and are important to include in CM optimization problems. The constraint sensitivity for the volume constraint is straightforward and can be written as:

$$\frac{\partial V}{\partial \boldsymbol{\rho}} = 1. \tag{3.23}$$

3.1.6. Regularizations

Different regularizations tools or techniques are used to ensure feasible results. A common one is filtering, which prevents checkerboard designs [65, 66, 67]. The classical density filter [68, 69] helps prevent this error. The filtered design variable $\tilde{\rho}_e$ for element e is the weighted average of the design variable ρ_j and is determined as:

$$\tilde{\rho}_e = \frac{\Sigma_{j=1}^{N_e} v_j w(\mathbf{x})}{\Sigma_{j=1}^{N_e} w(\mathbf{x})}\rho_j, \tag{3.24}$$

where N_e represents the total number of elements that lie within the filter radius R_{fill} for the eth element, v_j is the volume of the the jth element and $w(\mathbf{x})$, the weight function, is defined as:

$$w(\mathbf{x}) = \max\left(0, 1 - \frac{||\mathbf{x}_i - \mathbf{x}_j||}{R_{\text{fill}}}\right), \tag{3.25}$$

where ||$\mathbf{x}_i$-$\mathbf{x}_j$|| is the Euclidean distance between the eth and jth elements. $\mathbf{x}_i$ and $\mathbf{x}_j$ indicate the center coordinates of the eth and jth elements, respectively. The derivative of filtered density with respect to the design variable can be evaluated as:

$$\frac{\partial \tilde{\rho}_i}{\partial \rho_j} = \frac{\Sigma_{j=1}^{N_e} v_j w(\mathbf{x})}{\Sigma_{j=1}^{N_e} w(\mathbf{x})}. \tag{3.26}$$

The values of v_j and $w(\mathbf{x})$ do not change with iterations and can therefore be stored in a vector **Hs**. Post filtering, the old design vector $\boldsymbol{\rho}$ is replaced by the new design vector $\tilde{\boldsymbol{\rho}}$. Every element has a filtered density value $\tilde{\rho}_e$ and every density dependent function is now dependent on the filtered density value. The derivative or sensitivities of any such function C can be determined through the chain rule as:

$$\frac{\mathrm{d}C}{\mathrm{d}\rho} = \frac{\mathrm{d}C}{\mathrm{d}\tilde{\boldsymbol{\rho}}} \frac{\mathrm{d}\tilde{\boldsymbol{\rho}}}{\mathrm{d}\boldsymbol{\rho}}. \tag{3.27}$$

Another tool that is used to ensure symmetric designs in the design space, is symmetric sensitivity averaging. By symmetrically averaging the sensitivities it is possible to obtain symmetric results about planes, lines, or a point [70]. Mathematically,

$$S_e = \frac{\Sigma_{i \in A_e} S_i}{N}, \tag{3.28}$$

where S_e denoted the sensitivity value of element e and A_e is a set of element numbers that is symmetric to element e. It is important to note that $i \in A_e$. For the 3D case, the elements are chosen symmetrically to a point as shown in Fig. 3.8.

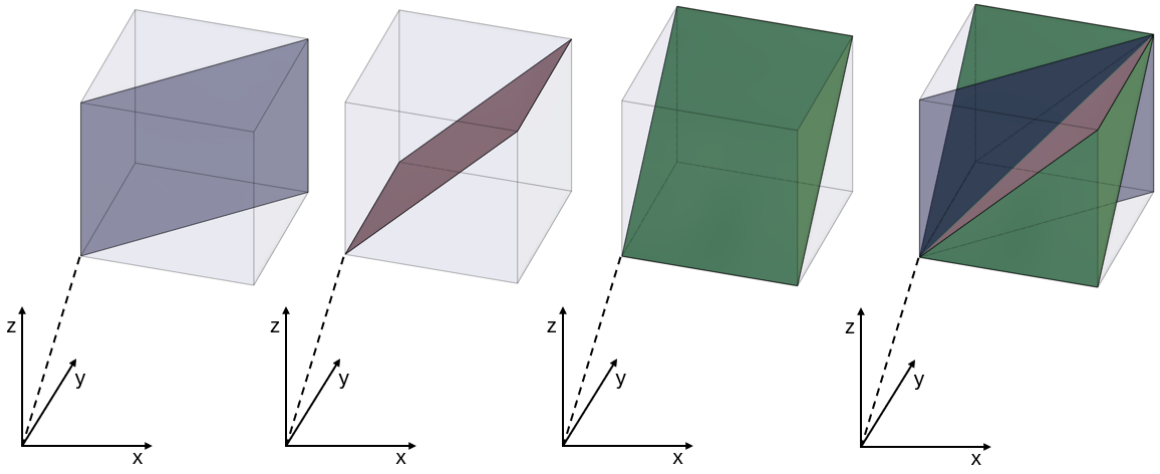

Figure 3.8: A schematic representation of the symmetry applied in the 3D case. Three symmetric planes (blue, red and green) are applied altogether giving it a symmetry about the diagonal passing from the origin to the diagonally opposite point.

To find the symmetric elements for this case, the x, y and z coordinates of each element are calculated and every combination of those values belongs to one set. Mathematically,

$$A_{e_{ijk}} = \{e_{ijk},\ e_{ikj},\ e_{jik},\ e_{kij},\ e_{jki},\ e_{kji}\}, \tag{3.29}$$

where i, j and k denote the x, y and z coordinates of element e. Examples of some related elements are visualized in Fig. 3.9.

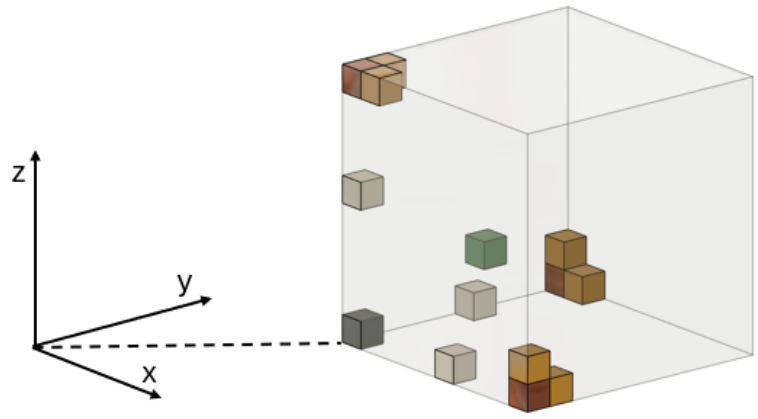

Figure 3.9: Schematic representation of different symmetric element examples using the method described in Eq. 3.29. The elements with the same colors belong to one symmetric set.

Passive elements are chosen depending on the case. The density of these elements does not change after any iterations. All the elements touching the face of the output nodes, except the elements containing the output nodes, are chosen as passive void elements ($\rho = 0$) while the elements containing the output nodes are chosen as passive solid elements ($\rho = 1$). The passive solid elements are created to ensure connectivity with the other unit cells, while the passive void elements are created to minimize parasitic motion and to avoid any contact after deformation. This is further illustrated in Fig. 3.10

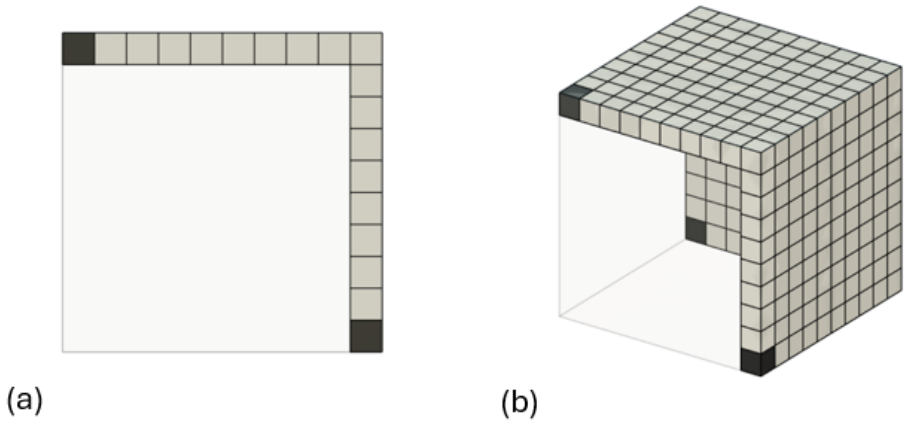

Figure 3.10: **(a)** Passive elements for every 2D cell. **(b)** Passive elements required for every 3D unit cell. Dark gray elements are passive solid elements while light gray elements are passive void elements.

3.2. Optimization Problem

The optimization problem required for the NLC metamaterial design case can be written by taking into account the objective equation (Eq. 3.2), the state equations (Eqs. 3.3, 3.12, 3.16) and the constraints (Eq. 3.17). Mathematically,

$$\left.\begin{aligned} \min_{\tilde{\rho}} \quad & : -\frac{MSE(\mathbf{u},\mathbf{v},\tilde{\boldsymbol{\rho}})}{2SE(\mathbf{u},\tilde{\boldsymbol{\rho}})} \\ \text{s.t.} \quad & : \mathbf{Ap} = 0 \\ & : \mathbf{Ku} = \mathbf{F} = -\mathbf{Hp} \\ & : \frac{V(\tilde{\boldsymbol{\rho}})}{V_0 \boldsymbol{f}} \leq 1 \\ & : 0 \leq \tilde{\boldsymbol{\rho}} \leq 1 \end{aligned}\right\}. \tag{3.30}$$

Note, ρ is replaced by $\tilde{\rho}$ as the design variable, since density filtering is applied to these design problems. This optimization problem is consistent for all the design cases discussed in this thesis. In 2D cases, however, the state equations have to be slightly adapted. The calculation of these equations are detailed in Kumar et al. [56].

3.3. Design-independent Isotropic NLC Unit Square

The simplest design case for an NLC unit cell is a 2D design-independent[1] unit square. Due to symmetry, one quarter of the total unit square is selected as the TO design domain, this is indicated in Fig. 3.2. The design layout consists of a passive void square, in the bottom-left corner of the design space that is completely enclosed by solid passive elements. This passive void square contains the pressurized fluid which exerts a pressure force on the passive solid boundary enclosing it. This pressure boundary is design-independent and does not change as the design evolves. The boundary conditions are depicted in Fig. 3.11. An input pressure (p_{in}) is applied along the left and bottom sides of the passive void square and a non-pressurized boundary condition ($p = p_{\text{out}} = 0$) is applied to the right and top side of the design domain. Symmetric boundary conditions that prevent displacement in the direction normal to the boundary are applied on the left and bottom sides of the design domain. The nodes corresponding to the top-left and bottom-right corners of the design domain are chosen as output points. Finally, additional passive regions are chosen similar to Fig. 3.10.

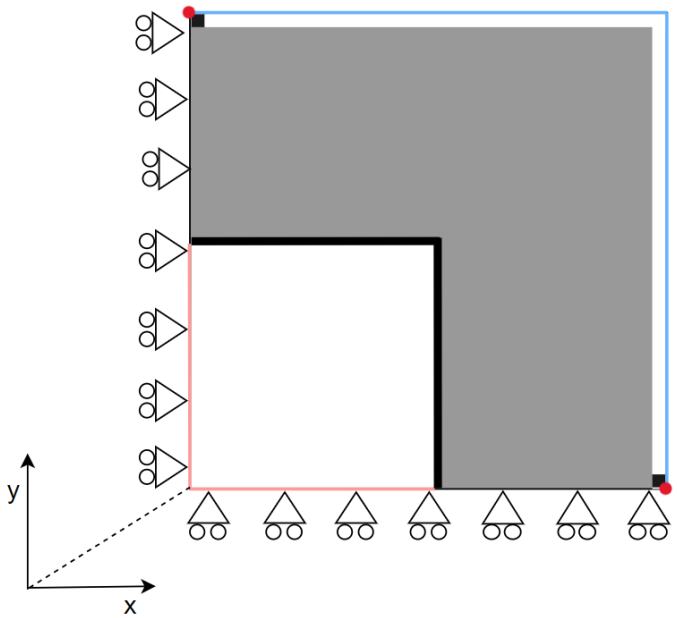

Figure 3.11: Schematic representation of the design-independent isotropic NLC unit square. Illustrating input (red) and non-pressure (blue) boundaries. The symmetric displacement pressure boundary is labeled as roller constraints. Lastly, the passive solid (black), void regions (white), and the output points (red dot) in the design domain (gray) are illustrated.

Table 3.1 details the various parameter values for this design case.

1 The term design-independent has been used to indicate that the pressure boundary is design-independent.

Domain Parameters	Values	Boundary Parameters	Values
Side length of domain (L)	100 mm	Modulus of solid material (E_0)	1650 MPa
Elements along one axis	100	Poisson's ratio of material (ν)	0.35
Thickness of square (T_s)[2]	1 mm	Modulus of void material (E_{min})	1650 $\times$ 10^{-6} MPa
Passive square length (S_c)	50 mm	Penalization (γ)	3
Passive square thickness (S_t)	2 mm	Output spring stiffness (k_{ss})	0.1 Nmm
Density filter radius (R_{fill})	2 mm	Input pressure (p_{in})	0.3 MPa
Volume fraction (f)	0.1	Output pressure (p_{out})	0 MPa
Optimization Parameters	**Values**	**Darcy Parameters**	**Values**
MMA constant a_0	1	Flow coefficient of void (k_{v})	1 $mm^4N^{-1}s^{-1}$
MMA constant a_i	0	Flow coefficient of solid (k_{s})	1×10^{-7} $mm^4N^{-1}s^{-1}$
MMA constant c_i	1000	Pressure drop ratio (r)	0.1
MMA constant d_i	0	Penetration depth (Δs)	2 mm
Density move limit ($\Delta\rho$)[3]	0.1	Heaviside slope parameter ($\beta_{\text{k}}/\beta_{\text{h}}$)	10
Maximum iterations	500	Heaviside step parameter ($\eta_{\text{k}}/\eta_{\text{h}}$)	0.1
Normalization scalar[4]	1000	Initial pressure (p_{initial})[5]	1×10^{-5} MPa

Table 3.1: Input parameters for the density-based optimization of a design-independent isotropic NLC unit cube.

Most of the domain parameter values, maximum iterations, and boundary parameter values are selected arbitrarily. In contrast, the optimization parameter values, such as density filter radius R_{fill}, the "Darcy Method" parameter values, penalization, and output stiffness k_{ss} are selected based on literature, considering the design resolution and dimensions [63, 60, 18, 61, 59]. Finally, a convergence limit of 0.01 is also specified. This means that the optimizer will stop iterating either if the maximum absolute difference between the old and updated design variables falls below the convergence limit or if the maximum number of iterations is reached.

3.4. Design-independent Isotropic NLC Unit Cube

This design case is the 3D equivalent of the design-independent NLC unit square. Due to symmetry, one-eighth of the total unit cube is selected as the TO design domain, this is indicated in Fig. 3.2. The passive void square is replaced by a passive void cube that is enclosed by a passive solid region. The pressurized fluid is contained in the void region and applies a pressure force on the inner walls of the solid region.

Input pressure is applied on the walls of the void region that touches the front, left, and bottom face of the design domain and the right, top, and back faces of the design space are selected as non-pressurized boundary faces with additional passive regions being applied around it, similar to Fig. 3.10. The faces mentioned above are labeled in Fig. 3.12.

Symmetric boundary conditions that prevent displacement in the direction normal to the boundary are applied on the left, front, and bottom faces of the design domain. Finally, the output points are selected as the nodes corresponding to the top-front-left, the bottom-front-right, and the bottom-back-left corners of the design space. The passive regions, pressure faces and output points are indicated in Fig. 3.13. Note: Sensitivity averaging is used in the 3D case, as visualized in Fig. 3.8.

2 Thickness required for the plane stress case.
3 This is an MMA parameter that defines the change in density in each optimization iteration.
4 This scalar is multiplied to the objective, constraint and sensitivity values to prevent early convergence.
5 This is the initial nodal pressure, set before any iterations to prevent singularity problems.

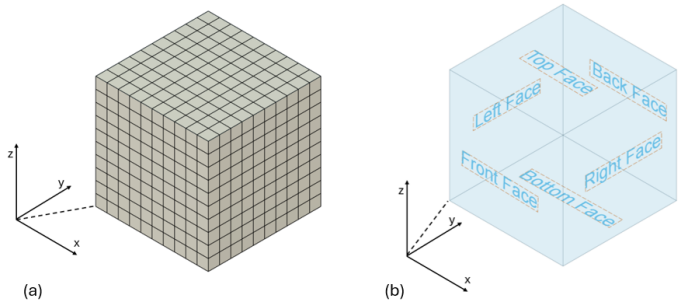

Figure 3.12: **(a)** Discretized design domain of the an NLC unit cube. **(b)** The 3D design domain and its different faces labeled.

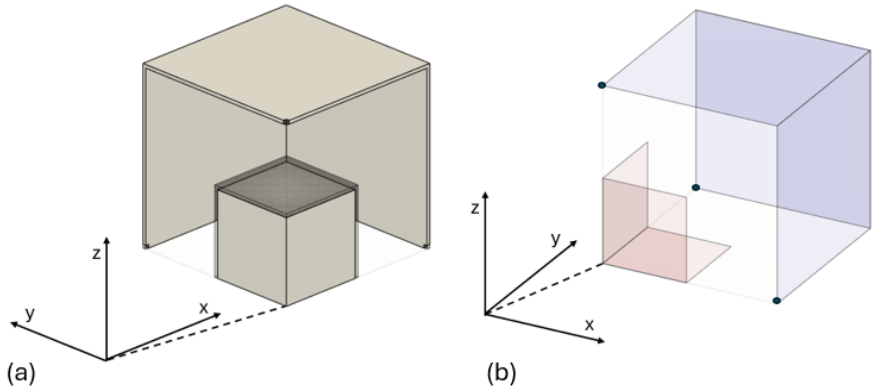

Figure 3.13: **(a)** Schematic representation of passive solid (dark gray and translucent) and the passive void (light gray) regions. **(b)** Schematic representation of the input pressure (red), non-pressurized faces (blue), and output points (black dot).

Most of the parameters, including the convergence criteria, are maintained the same as in Table 3.1. The different/additional parameters are given in Table 3.2.

Domain Parameters	Values	Boundary Parameters	Values
Side length of domain (L)	50 mm	Modulus of solid material (E_0)	3000 MPa
Elements along one axis	50	Poisson's ratio of material (ν)	0.4
Elemental side length (D)	1 mm	Modulus of void material (E_{min})	3000 $\times$ 10^{-6} MPa
Volume fraction (f)	0.1	Output spring stiffness (k_{ss})	10 Nmm
Density filter radius (R_{fill})	1.5 mm	Input pressure (p_{in})	0.1 MPa
Optimization Parameters	Values	Darcy Parameters	Values
MMA constant c_i	10000	Initial pressure (p_{initial})	1 $\times$ 10^{-4} MPa

Table 3.2: Input parameters for the density-based optimization of a design-independent isotropic NLC unit cube.

The side length of the passive void region and the thickness of the passive solid region encompassing it are selected as 35 mm and 2 mm, respectively. These values, along with the side length of the domain and the material parameters, are chosen to match the dimensions and material used in the design by Qu et al. [8], as the design obtained in this study will be compared to theirs. The reasoning behind the values of the other parameters is similar to that used in the equivalent 2D case.

3.5. Isotropic NLC Unit Square

The pressure loads in the isotropic NLC unit square case are design-dependent. No predetermined passive regions enclosing the fluid have been set, allowing the optimizer to create its own topology to enclose the pressurized fluid, hereby referred to as the pressurized shell.

Apart from the absence of a passive void square and its enclosing passive solid region, the only difference between the design-independent and design-dependent isotropic NLC unit squares is the definition of their input pressure boundaries. In this case, the input pressure boundary is defined as the bottom and left sides of the design domain. This is visualized in Fig. 3.14.

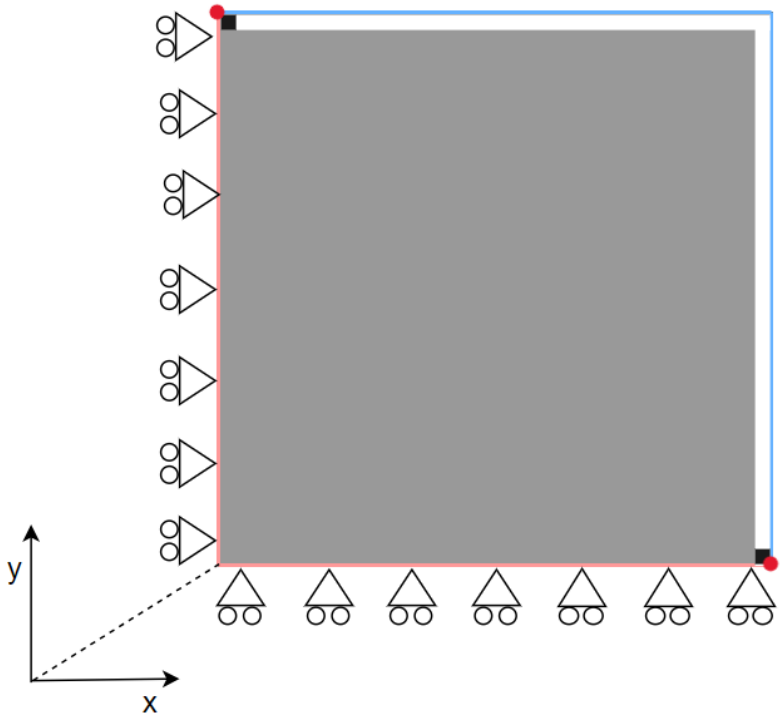

Figure 3.14: Schematic representation of the isotropic NLC unit square. Illustrating input (red) and non-pressure (blue) boundaries. The symmetric displacement pressure boundary is labeled as roller constraints. Lastly, the passive solid (black), void regions (white), and output points (red dot) in the design domain (gray) are illustrated.

All the required parameters are defined in Table 3.1 and a convergence limit of 0.01 is also specified.

3.6. Isotropic NLC Unit Cube

This design case is the 3D equivalent of the design-independent NLC unit square, similar to the design-independent NLC unit square the pressure loads are design-independent. No predetermined passive regions enclosing the fluid have been set, allowing the optimizer to create its own pressurized shell. This statement is not entirely true however. An inlet region has to be set to allow pressure to flow through the system and give feasible results.

This region does influence the shape of the final pressurized shell. In this case, circular inlet regions have been selected.[6] Each inlet region consists of a circular quadrant, centered at the front-bottom-left corner of the design domain. There are three quadrants in total: one along the bottom face, another along the left face, and the last one along the front face. These quadrants form the input pressure faces of the design. The output pressure faces remain the same as in the design-independent case. This is further illustrated in Fig. 3.15.

6 The circular shape has been chosen as it is symmetric.

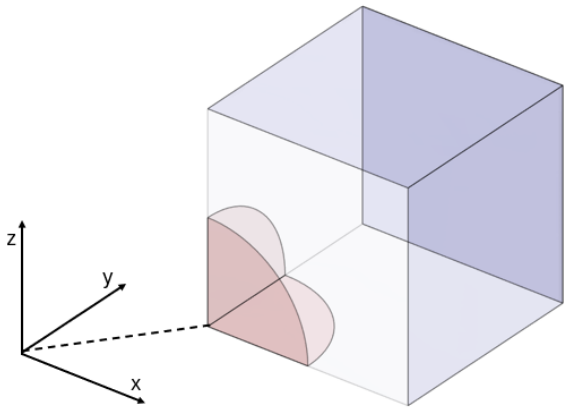

Figure 3.15: Schematic representation of the input pressure region (red) and the non-pressurized faces (blue) of the isotropic NLC unit cube.

To prevent the inlet face from changing, an element thick passive void region is placed above every inlet face. These void regions are further enclosed by passive solid regions. This along with the additional passive region (Fig 3.10) is further illustrated in Fig. 3.16.

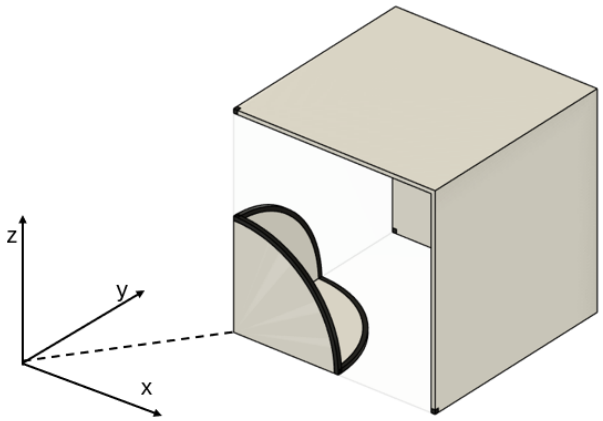

Figure 3.16: Schematic representation of the passive elements of the isotropic NLC unit cube. The passive void elements (beige) and the passive solid elements (black).

Lastly, most of the required parameter values remain the same as in the design-independent case. New material parameter values for the modulus of solid material E_0, Poisson's ratio of the material ν, and the modulus of void material E_{min} are selected as 75 MPa, 0.38 and 75 $\times$ 10^{-6} MPa, respectively. These parameters are chosen based on the material used for manufacturing. A similar convergence limit is set, and sensitivity averaging is implemented. The radius of the passive quadrant is 25 mm, while the thickness of the solid region enclosing it is set to 2 mm, these dimensions are selected arbitarily.

3.7. Design Validation Method

The isotropic NLC unit cube design is validated using a FE simulation software called COMSOL and an experimental setup that measures the displacement of the output under an increase in internal pressure. The obtained results are converted to an stereolithography (STL) file made up of iso-surface facets with a density threshold of 0.5.

3.7.1. COMSOL Study

For the numerical study in COMSOL, the design obtained from TO is divided along the planes of symmetry to ensure faster and easier computation. Symmetric boundary conditions are applied on these planes, that prevent any displacement in the direction normal to the plane. The other planes of symmetry, that were defined in the TO problem also have a similar boundary condition imposed on them. These are the planes that divide the entire unit cube into eight part. Finally, a uniform pressure force of 0.1 MPa is applied internally along the walls that contain the pressurized fluid.

A stationary solid mechanics study is chosen and the domain is discretized into elements. The Young's modulus and Poisson's ratio are maintained similar to the material parameters chosen in the optimization study. These match the properties of the material used to manufacture the design for experimental testing.

3.7.2. Experimental Setup

The overall unit cell is manufactured using selective laser sintering and flexible TPU is chosen as the material due to its flexible nature. The material parameters in the optimization are chosen to match the material properties of this material. Three laser interferometers are placed to measure the displacements in the x, y, and z direction. The stage is designed according to the obtained design as it needs to hold the unit cell in place without restricting the movement of the end points. Finally, an internal pressure of 0.1 MPa is applied through a pneumatic push-in connector that is attached to the unit cell through a threaded hole in the part of the design that experiences the pressure loads. The setup is shown in Fig. 3.17.

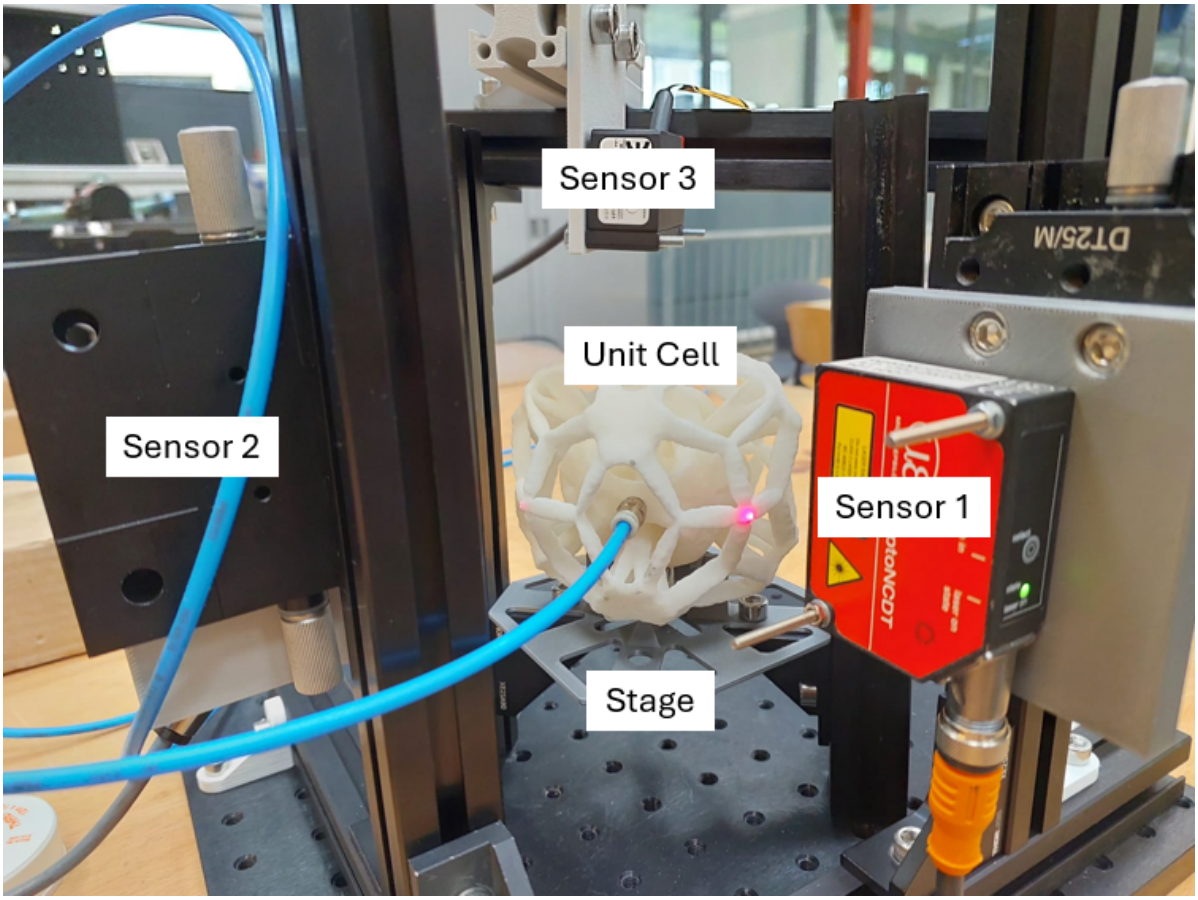

Figure 3.17: Experimental setup with stage and sensors. The blue pneumatic pipe is connected to a push-in connector that helps supply air which leads to an increase in pressure within the unit cell.

4

Results and Discussions

4.1. Design-independent Isotropic NLC Unit Square Design

The first result obtained was for the design-independent isotropic NLC unit square case. The design reached its convergence limit and stopped iterating after 327 iterations. The obtained design, along with the deformed (not to scale) design under an internal pressure of 0.3 MPa, are observed in Fig. 4.1.

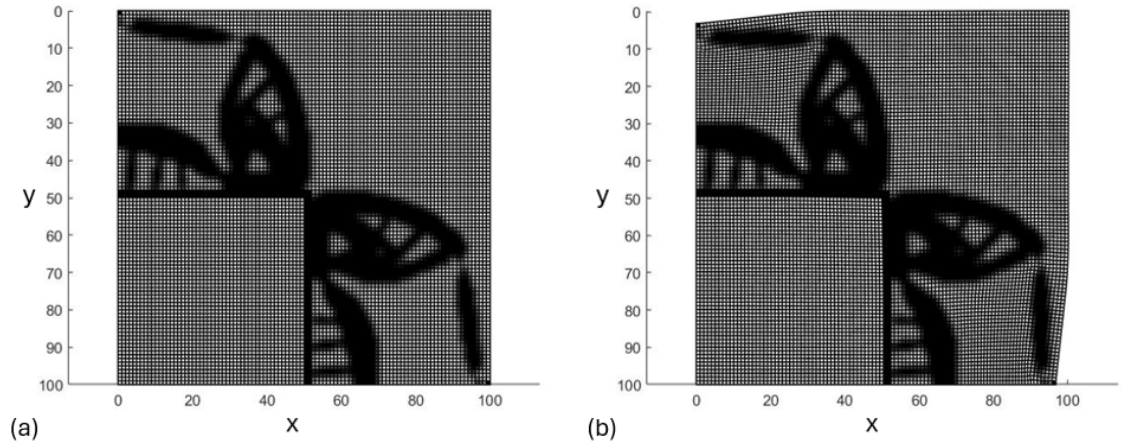

Figure 4.1: (a) Undeformed design-independent isotropic NLC unit square design. **(b)** Deformed design-independent isotropic NLC unit square design under an internal pressure of 0.3 MPa. Note: The deformation is not to scale.

From the deformed result it can be observed that the inflation of the passive square region rotates the arms towards the corner of the square due to the large bending displacement in the middle of the square region. Ultimately leading to a negative displacement along both both the axis at the output points. The length of the design is 100 mm and it is optimized for an internal pressure of 0.3 MPa. Applying this pressure condition results in a displacement of -7.112 mm and a linear compressibility value of:

$$K_L = -\frac{1}{L}\left(\frac{dL}{dP}\right)_T = -\frac{1}{100}\left(\frac{-7.112}{-0.3}\right)_T = -0.237\ \text{MPa}^{-1} = -2.370\ \%/\text{bar}. \tag{4.1}$$

The design exhibits a decent NLC value; however, it is important to note that this NLC value differs and is larger than the NLC value exhibited by the overall metamaterial composed of an array of similar unit cells.

4.2. Design-independent Isotropic NLC Unit Cube Design

The second result obtained was for the design-independent isotropic NLC unit cube case. The design didn't reach its convergence limit but ended after reaching the maximum iteration value, 500 iterations[1]. However, a feasible result[2] for the design-independent NLC unit cube design is obtained. This result can be visualized in Fig. 4.2.

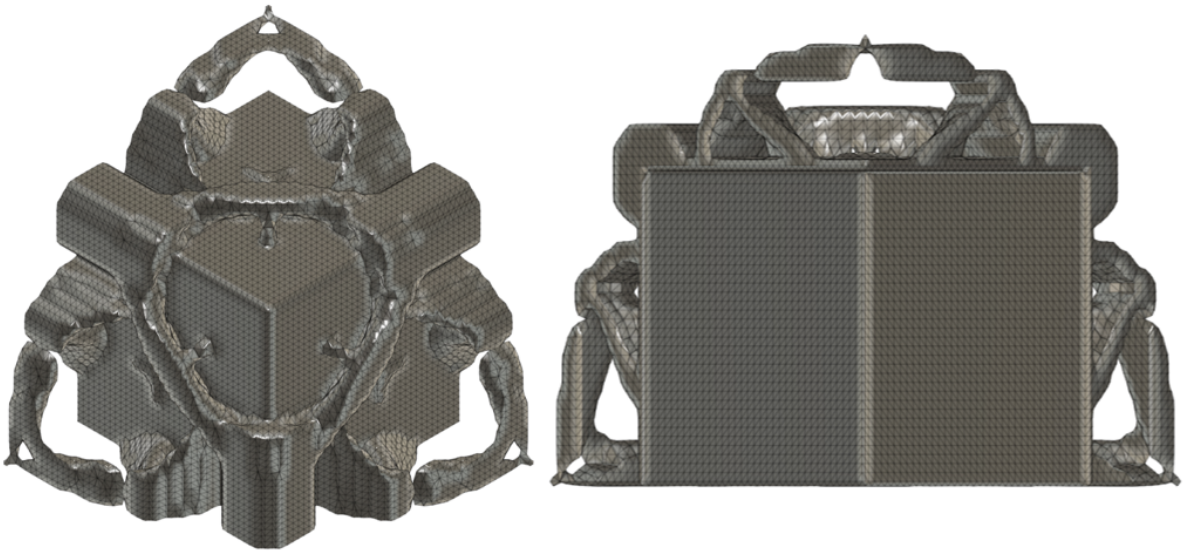

Figure 4.2: Different views of the obtained design-independent isotropic NLC cube design.

The pressurized fluid is within in the passive cube that inflates when pressure is applied. This leads to the arms being pushed towards the corner of the cube. This is caused due to the uneven bending displacement of the cubic walls, Ultimately leading to an overall compression of the unit cell. This deformation can clearly be observed in Fig. 4.3.

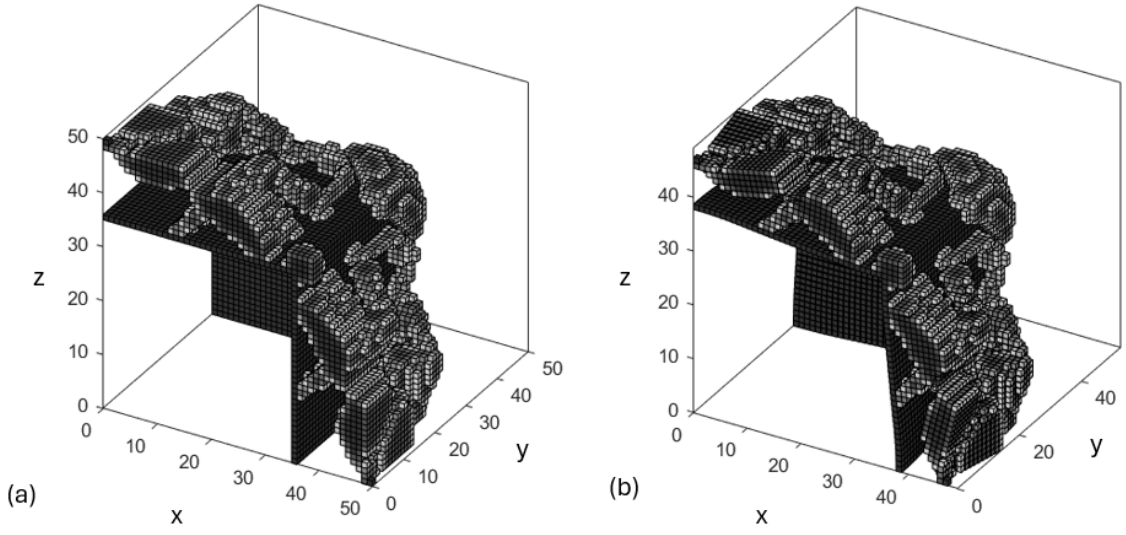

Figure 4.3: (a) Undeformed design-independent isotropic NLC design. **(b)** Deformed design-independent isotropic NLC design after an application of 0.1 MPa. Note: The deformation is not to scale.

The length of the design is 50 mm and it is optimized for an internal pressure of 0.1 MPa. Applying this

1 A higher iteration limit is computationally expensive and time consuming.
2 Feasible can be checked using a measure of non-discreteness. The lower the percentage the more discrete (black and white) the result. The measure of non-discreteness for this design is is 6.926%, indicating a discrete result [71].

pressure condition results in a displacement of -1.106 mm and a linear compressibility value of:

$$K_L = -\frac{1}{L}\left(\frac{dL}{dP}\right)_T = -\frac{1}{50}\left(\frac{-1.106}{-0.1}\right)_T = -0.221 \text{ MPa}^{-1} = -2.212 \text{ \%/bar}. \tag{4.2}$$

The obtained result has a decent NLC value, similar to its 2D counterpart and just like the 2D case, this NLC value differs and is larger than the NLC value exhibited by the overall metamaterial.

4.3. Isotropic NLC Unit Square Design

The third result obtained was for the isotropic NLC unit square case. The design reached its convergence limit and stopped iterating after 306 iterations. The obtained design, along with the deformed (not to scale) design under an internal pressure of 0.3 MPa, is observed in Fig. 4.4.

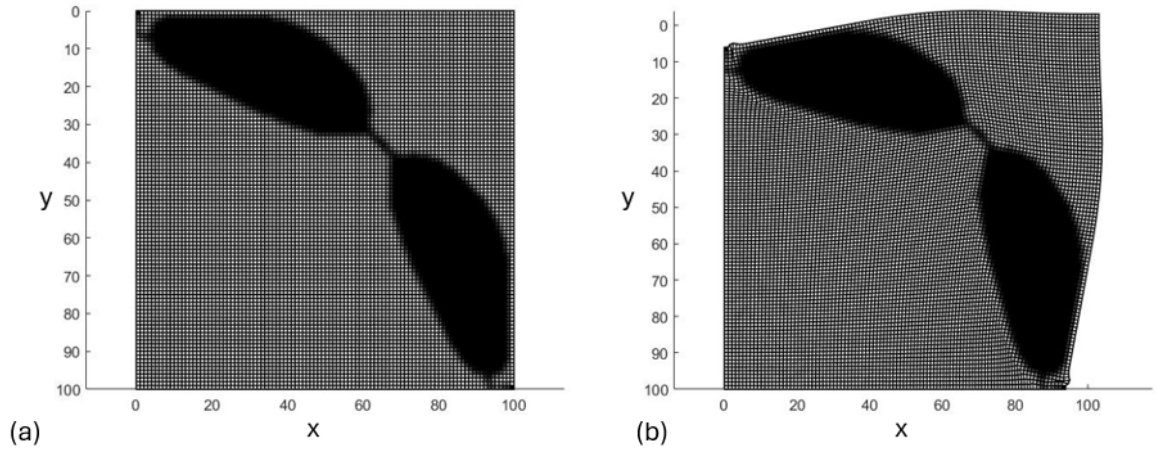

Figure 4.4: (a) Undeformed isotropic NLC unit square design. **(b)** Deformed isotropic NLC unit square design under an internal pressure of 0.3 MPa. Note: The deformation is not to scale.

It is a symmetric design with a circular pressurized shell that is thinnest in the middle. The thinnest part of the shell forms a hinge connecting the two output points. The rotation of this thin hinge upon inflation leads to an inward rotation of the thicker part of the shell, ultimately leading to a negative displacement. The length of the design is 100 mm and it is optimized for an internal pressure of 0.3 MPa. Applying this pressure condition results in a displacement of -10.104 mm and a linear compressibility value of:

$$K_L = -\frac{1}{L}\left(\frac{dL}{dP}\right)_T = -\frac{1}{100}\left(\frac{-10.104}{-0.1}\right)_T = -0.337 \text{ MPa}^{-1} = -3.367 \text{ \%/bar}. \tag{4.3}$$

The obtained result has a higher NLC value when compared to the design-independent case. Just like the design-independent case, this NLC value differs and is larger than the NLC value exhibited by the overall metamaterial.

4.4. Isotropic NLC Unit Cube Design

The second result obtained were for the design-independent isotropic NLC unit cube case. The design didn't reach its convergence limit but ended after reaching the maximum iteration value, 500 iterations. However, a feasible result[3] for the design-independent NLC unit cube design is obtained. This result can be visualized in Fig. 4.5.

It can be observed that the preset passive solid region forms a spherical pressurized shell that traps the pressure and inflates. The output displacement is not caused entirely due to the inflation of this spherical shell but rather through the pressure acting on the bulge in the middle. This bulge is thin in

3 Measure of non-discreteness is 9.697%, indicating a discrete result [71].

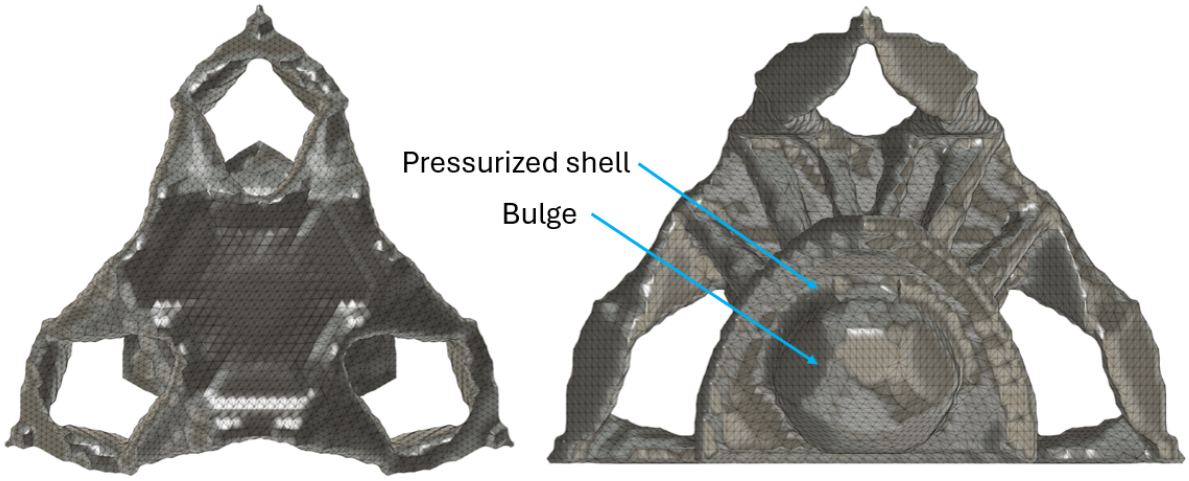

Figure 4.5: Different views of the obtained isotropic NLC cube design.

thickness and forms a cavity in the circular shell. The deformation in this bulge pushes the back of the unit cell, which connects all six arms together. This leads to the equal rotation of the six arms into the middle of the unit cell, ultimately leading to an equal negative displacement in all three directions which results in isotropic NLC behavior. The design under deformation can be observed in Fig. 4.6.

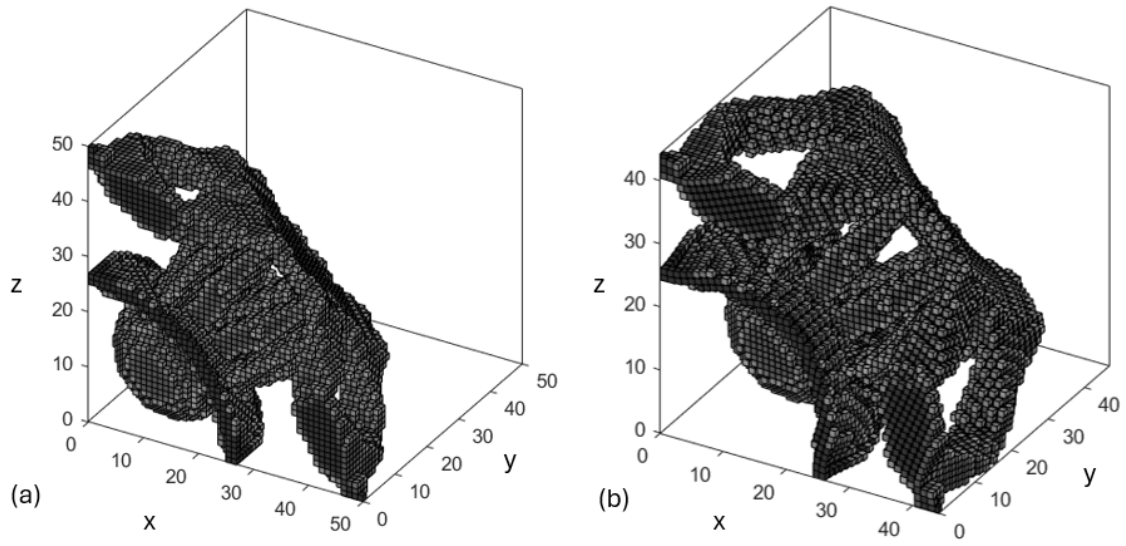

Figure 4.6: **(a)** Undeformed isotropic NLC design. **(b)** Deformed isotropic NLC design after an application of 0.1 MPa. Note: The deformation is not to scale.

The length of the design is 50 mm and it is optimized for an internal pressure of 0.1 MPa. Therefore, applying this pressure condition results in a displacement of -1.761 mm and a linear compressibility value of:

$$K_L = -\frac{1}{L}\left(\frac{dL}{dP}\right)_T = -\frac{1}{50}\left(\frac{-1.761}{-0.1}\right) = -0.353\ \text{MPa}^{-1} = -3.534\ \%/\text{bar}. \tag{4.4}$$

The obtained result has a higher NLC value when compared to the design-independent case and a value similar its 2D counterpart. Just like the design-independent and 2D case, this NLC value differs and is larger than the NLC value exhibited by the overall metamaterial.

4.5. Parameter Study

Some of the TO parameters were selected arbitrarily, therefore a parameter study is performed on some of the arbitrarily selected TO parameters. This study is performed on the 2D case as a parameter study on the 3D case is computationally expensive.

The first parameter study was conducted on three parameters in the design-dependent 2D case. The parameters chosen were volume fraction *f*, output spring stiffness k_{ss}, and input pressure p_{in}. The obtained NLC results along with the parameter values are illustrated in Fig. 4.7.

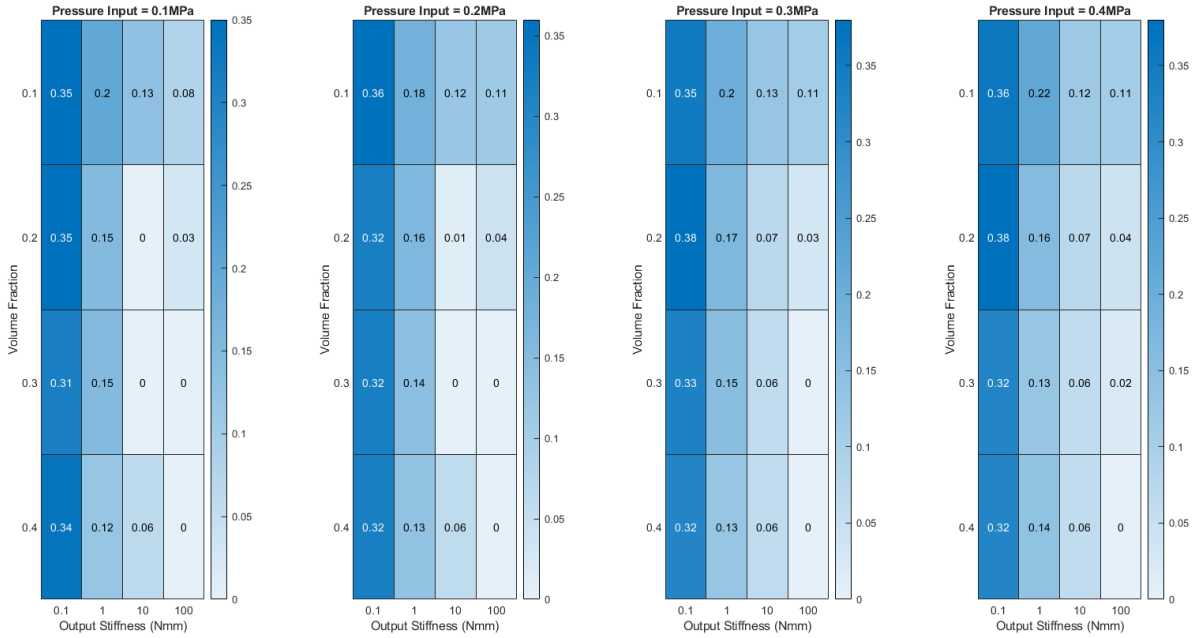

Figure 4.7: Heatmaps of NLC Values for different pressure input.

The second parameter study was conducted on three parameters in the design-independent 2D case. All three parameters are related to the passive region that encloses the fluid. The first one is the shape of the region; quadrant, square or triangle[4]. The second parameter is the defining length of the shape. For the square it is the side length, radius for the circle and side length (not the hypotenuse) for the triangle. The last parameter is the thickness of the passive solid region enclosing it. The shapes and parameters can be better visualized in Fig. 4.8.

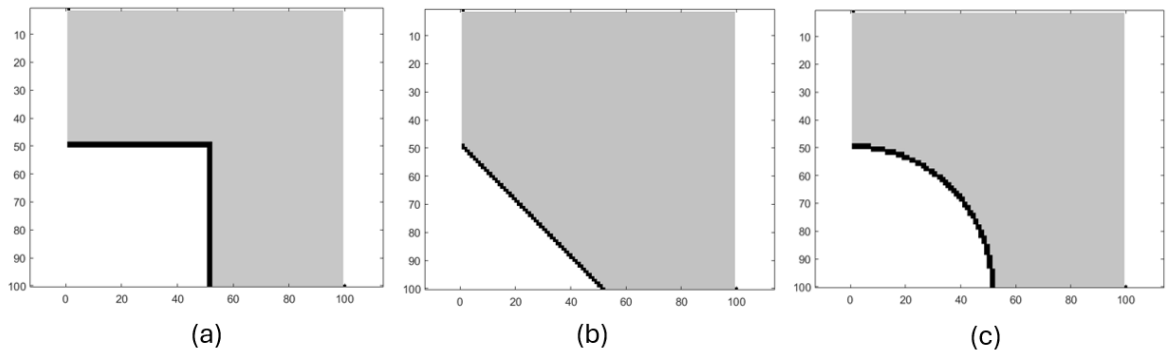

Figure 4.8: Initial design domain for the different passive region shapes: **(a)** Square. **b** Triangle. **(c)** Quadrant.

4 The triangle passive region forms a 45 degrees-rotated square when all symmetric quarters of the unit cell are assembled together.

The obtained NLC results along with the parameter values are illustrated in Fig. 4.9.

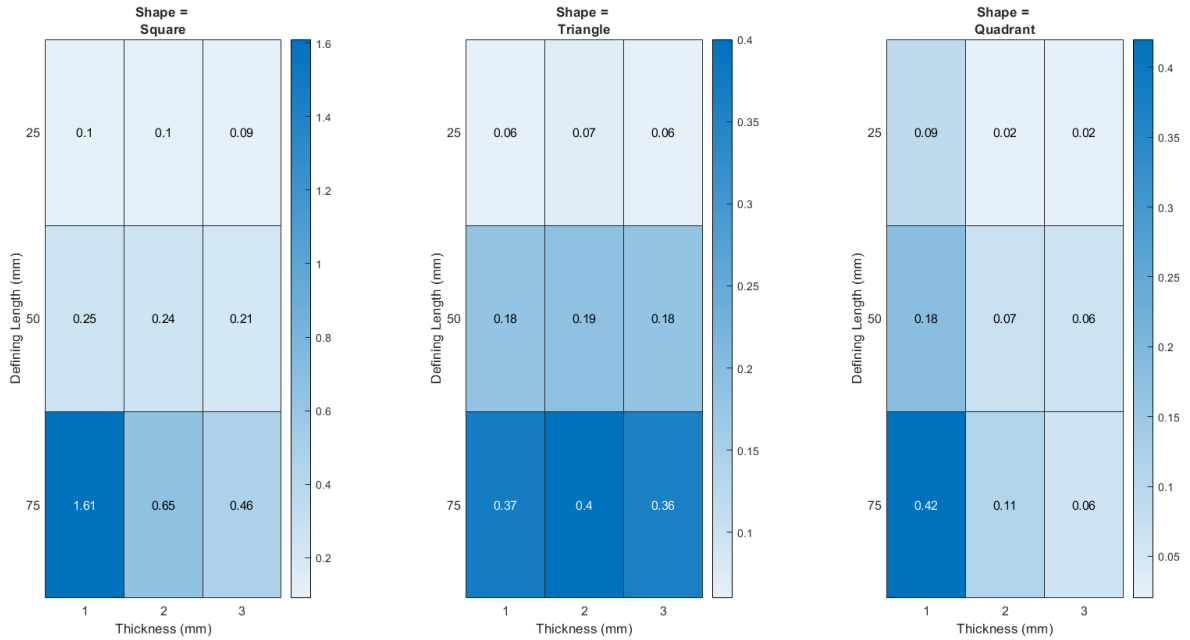

Figure 4.9: Heatmaps of NLC Values for different passive shape.

From the first parameter study it is observed that in general a greater NLC value is obtained with a lower volume fraction, a lower output stiffness and a higher input pressure value. Among the 64 combination the best NLC value is obtained for a design with a volume fraction of 0.2, an output stiffness of 0.1 Nmm, and an input pressure of 0.4 MPa. From the second parameter study it is observed that in general a greater NLC value is obtained with a square shape, a higher defining length and a lower thicknes svalue. Among the 27 combination the best NLC value is obtained for a design with a square passive region with a defining length of 75 mm, and an thickness of 1 mm.

4.6. Comparative Study

4.6.1. Darcy Method Comparison

Although the “Darcy method” is clearly advantageous over other pressure load application methods, due to the inclusion of load sensitivities [56], we want to test whether a simplistic pressure load application approach can be implemented for a design-independent problem.

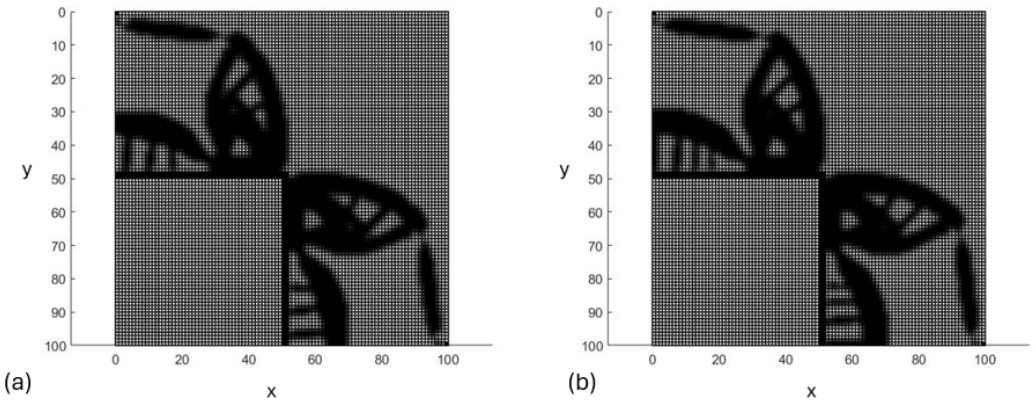

Figure 4.10: **(a)** Design-independent isotropic NLC unit square design resulting from the “Darcy Method”. **(b)** Design-independent isotropic NLC unit square design resulting from the standard method.

This can be explored by a comparative study between the “Darcy Method” and a standard method; i.e., a standard CM synthesis problem [61], where boundary forces are applied at the start on every node perpendicularly to the direction of the pressure boundary. The magnitude of each individual force vector can be determined by dividing the product of the total area and pressure with the total number of nodes on that surface. As observed in Fig. 4.10, the two designs are similar.

The standard method design has an output displacement value of -7.1525 mm while the “Darcy Method” design has an output displacement value of -7.112 mm when a pressure of 0.3 MPa is applied. Therefore, a claim can be made to implement the standard approach for design-independent problems as it is computationally inexpensive and easier to implement.

4.6.2. State of the Art Comparison

The closest existing designs (visualized in Figs. 2.6 and 2.7) to an isotropic NLC unit cube are the designs put forward by Qu et al. [8, 33]. The metamaterial exhibiting the higher NLC value (visualized in Fig. 2.7) between the two designs, has a volume compressibility value of -4.70 %/bar and a linear compressibility of -1.567 %/bar[5] [8]. This unit cell is however, designed either through intuition or through a trial and error approach. The TO methodology on the other hand, is systematic and capable of handling multiple complex restrictions while optimizing for various design parameters. Through this comparative study, we aim to demonstrate that it is possible to design a metamaterial unit cell with an NLC value greater than that of existing designs.

Qu et al. [8] provided the possibility of increasing the NLC value in the design, by changing dimensional parameters like the inner cube wall thickness, unit cell length, and inner cube length[6]. However, the fabrication of a thin wall is restricted by manufacturing limitations. It is difficult to identify the exact value of thickness that limits the design. However, the manufactured design by Qu et al.[8] has an inner wall thickness of 1.246 µm, a unit side length of 75 µm and an inner cube length of 52.5 µm. This is assumed to be the manufacturing limitation that limits the NLC value of the design and to ensure a fair comparison, the same dimensional limitations are taken into account for the TO methodology.

The output displacement value of the “existing design”[7] is computed using COMSOL. This is done by taking one-eighth of the total unit cell, applying a symmetric boundary condition on the planes of symmetry (the cell is divided similar to Fig. 3.2), and a uniform pressure load of 0.1 MPa on the walls of the inner cube. The deformation can be visualized in Fig. 4.11.

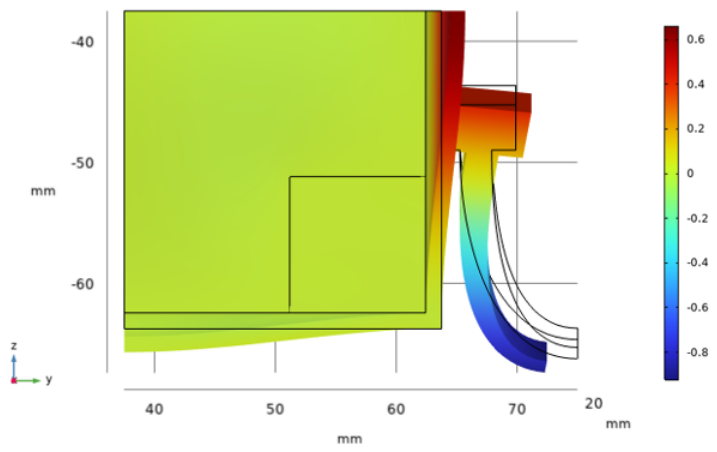

Figure 4.11: Contour plot of the deformed unit cell (Designed by Qu et al. [8]) and the wireframe plot describing the same unit cell when undeformed. The legend relates the contour colors to the deformation in the y direction, in millimeters.

5 The volume compressibility of an isotropic material is three times its linear compressibility.
6 The inner cube wall thickness, unit cell length, and inner cube length are labelled as t, a, and l in Fig. 2.7, respectively.
7 The design put manufactured by Qu et al. [8] is referred to as the “existing design” to ensure brevity of the report.

For an input pressure of 0.1 the simulated design has an output displacement of -0.922 mm. It should be noted that the design is simulated in the millimeter scale instead of the micrometer scale. This is done for a better comparison with the design obtained through TO[8]. Scaling the design does not have any affect on the compressibility values[9]. Using Eq. 1.1, the calculated linear compressibility is:

$$K_L = -\frac{1}{L}\left(\frac{dL}{dP}\right)_T = -\frac{1}{37.5}\left(\frac{-0.922}{-0.1}\right)_T = -0.246 \text{ MPa}^{-1} = -2.459 \text{ \%/bar}. \tag{4.5}$$

The length L is 37.5 mm because the unit cell is divided into eight parts, resulting in a length that is equal to half of the side length. It is also important to note that the linear compressibility value of -2.459 %/bar differs from the value of -1.567 %/bar stated by Qu et al. [8]. This is because the value put forward by Qu et al. is the linear compressibility exhibited by a four by four array constiting of the "existing design" unit cells. This is numerical simulated and can visualized in Fig. 4.12. The simulated array exhibits a total length increase of 0.461 mm and a thereby a linear compressibility of 1.537 %/bar for an array length of 300 mm and a input internal pressure of 0.1 MPa which is similar to the values put forward by Qu et al. [8].

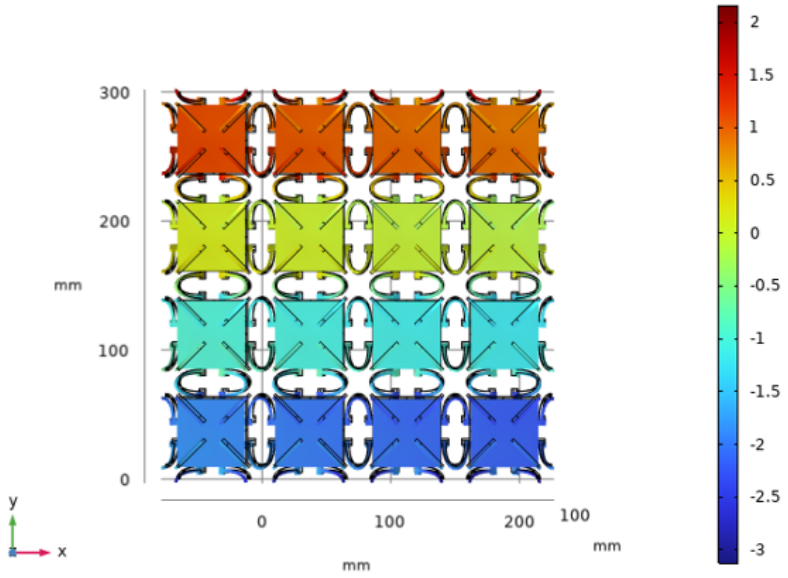

Figure 4.12: Contour plot of the deformed array (Designed by Qu et al. [8]). The legend relates the contour colors to the deformation in the y direction, in millimeters.

As mentioned in Section 3.4, the dimensional parameters for the TO-derived design were chosen based on the comparative study. The side length of the domain, the passive cube thickness, the passive cube length are chosen to be 50 mm, 2 mm, and 35 mm, respectively. As previously stated, scale does not affect the value of the linear compressibility. Uniform scaling down by a factor of 0.75 leads to a side half-length[10] of 37.5 mm and an inner cube half-length of 26.25 mm which is same as that of the simulated "existing design". The scaled inner cube wall thickness is 1.5 mm which is similar but not equal to the inner cube wall thickness of the "existing design".[11] As derived in Section 4.2, the design obtained

8 The computer-aided design (CAD) model of the "existing design" is easily scalable as compared to the design obtained through TO, which is complex (it contains many STL facets due to the large number of elements in the design space).

9 A numerical simulation of the design in the micrometer scale, using COMSOL, delivers the same NLC value.

10 It is denoted as half-length because it is half of the total length of the side length/inner cube length as the design is one-eighth of the total unit cell.

11 This is the closest value possible, as the discretization of the design domain limits us from selecting a thickness equal to that in the "existing design".

using the TO methodology displays an output displacement of -1.106 mm for an internal pressure of 0.1 MPa. Thus, exhibiting a linear compressibility value of -2.212 %/bar, which is similar but not more than the NLC value obtained from the “existing design”. However, TO possess several tools that can help further increase this displacement value. One of them is through a constraint on the overall strain energy SE [58]. The new optimization problem can be written as:

$$\left.\begin{aligned} \min_{\tilde{\rho}} \quad & : -u_{\text{out}} = -l^{\mathsf{T}}\mathbf{u} \\ \text{s.t.} \quad & : \mathbf{Ap} = 0 \\ & : \mathbf{Ku} = \mathbf{F} = -\mathbf{Hp} \\ & : \frac{V(\tilde{\boldsymbol{\rho}})}{V_0 \boldsymbol{f}} \leq 1 \\ & : \frac{SE(\tilde{\boldsymbol{\rho}})}{SE_0 \boldsymbol{k}} \leq 1 \\ & : 0 \leq \tilde{\boldsymbol{\rho}} \leq 1 \end{aligned}\right\}, \tag{4.6}$$

where *k* is the strain energy fraction that is a user-defined input that can be set to obtain higher output displacement values. SE_0 is the strain energy of the initial optimization stage and l is a vector with all zeros except the entry corresponding to the output degree of freedom, which is set to one. The value of *k* is chosen as 0.9 and constraint sensitivity is similar to the volume sensitivity [58]. The new objective sensitivity is as follows:

$$\frac{d\Phi}{d\tilde{\boldsymbol{\rho}}} = -l^{\mathsf{T}}\mathbf{K}^{-1}\frac{\partial \mathbf{K}}{\partial \tilde{\boldsymbol{\rho}}}\mathbf{u} + \underbrace{l^{\mathsf{T}}\mathbf{K}^{-1}\mathbf{H}\mathbf{A}^{-1}\frac{\partial \mathbf{A}}{\partial \tilde{\boldsymbol{\rho}}}\mathbf{p}}_{\text{Load sensitivities}}. \tag{4.7}$$

By constraining the SE, the optimizer is able to solely optimize the output displacement instead of the multi-criteria approach where the optimizer tries to find a balance between the MSE and SE value. The resulting design can be visualized in Fig. 4.13.

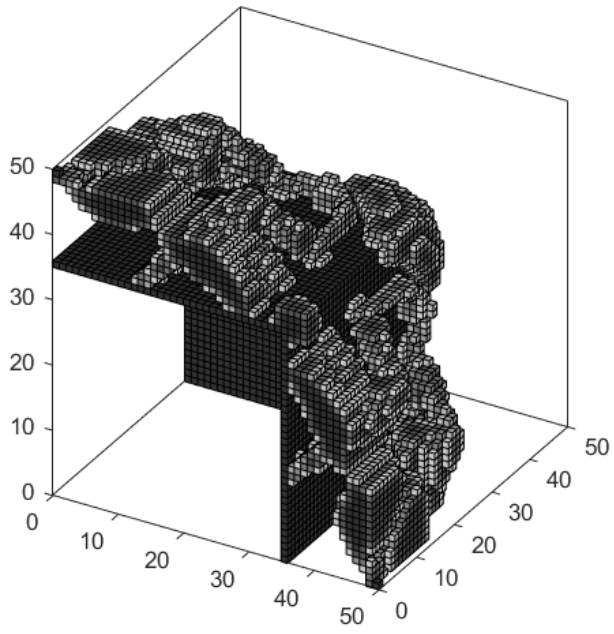

Figure 4.13: Strain energy constrained, design-independent NLC cube design.

The improved design has an output displacement value is -2.303 mm and linear compressibility value of:

$$K_L = -\frac{1}{L}\left(\frac{dL}{dP}\right)_T = -\frac{1}{50}\left(\frac{-2.303}{-0.1}\right)_T = -0.461 \text{ MPa}^{-1} = -4.606 \text{ \%/bar}. \tag{4.8}$$

Therefore, our design exhibits a larger NLC value compared to the design by Qu et al. [8], which has a linear compressibility value of -2.459 %/bar (the linear compressibility of the unit cell, not the metamaterial/array). This proves that the TO-driven methodology used in this study is not only a systematic design approach for NLC metamaterials but is also capable of achieving higher NLC values when compared to the state of the art designs.

4.7. Result Validation

The results from the COMSOL study show a linear displacement of -1.437 mm which is similar to the displacement value obtained in the optimization study. This can be visualized in Fig. 4.14.

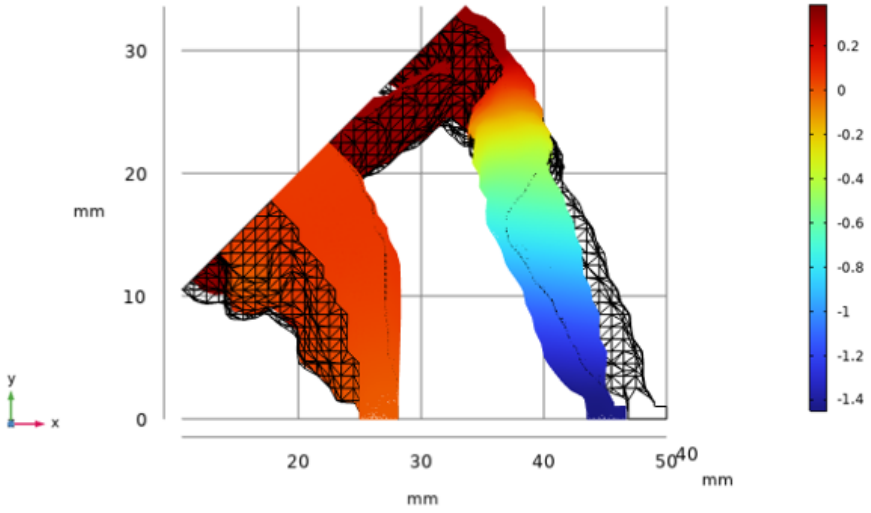

Figure 4.14: Contour plot of the deformed isotropic unit cell section along with the wireframe representation of its undeformed state. The legend relates the contour colors to the deformation in the x direction, in millimeters.

Th difference in value arises from the small changes in overall design while creating the STL. Setting of density threshold, changes in compliant hinges and addition of material to ensure continuity[12] are responsible for some of the discrepancies between simulations.

The results from the experimental setup (shown in Fig. 4.15) show a linear displacement of -1.350 mm and -1.253 mm in the horizontal directions while a displacement of -0.847 mm in the vertical direction. The two horizontal directions are similar to each other and the negligible difference between them can be related to either small inaccuracies in manufacturing, the human error in setting up the sensors (perpendicular to the output face) or unwanted rigid body motions, as the stage does not clamp the part but instead loosely holds it in place. There is, however, a larger difference between the displacements in the vertical and horizontal direction. This is due to the stage design for the experimental setup. The stage holds the design from the bottom and slightly prevents the proper inflation of the shell, even pushing it up a little bit. However, this is an experimental limitation and when rotated, the previously vertical output point (now along the horizontal direction) shows a displacement similar to the previously obtained horizontal displacement values. Therefore, it can be concluded that the design obtained is almost isotropic in nature exhibiting the same displacement along all the output points.

12 STL conversions lead to planar surfaces being converted into non-planar surfaces. These have to be reconstructed to ensure that the symmetric planes are maintained.

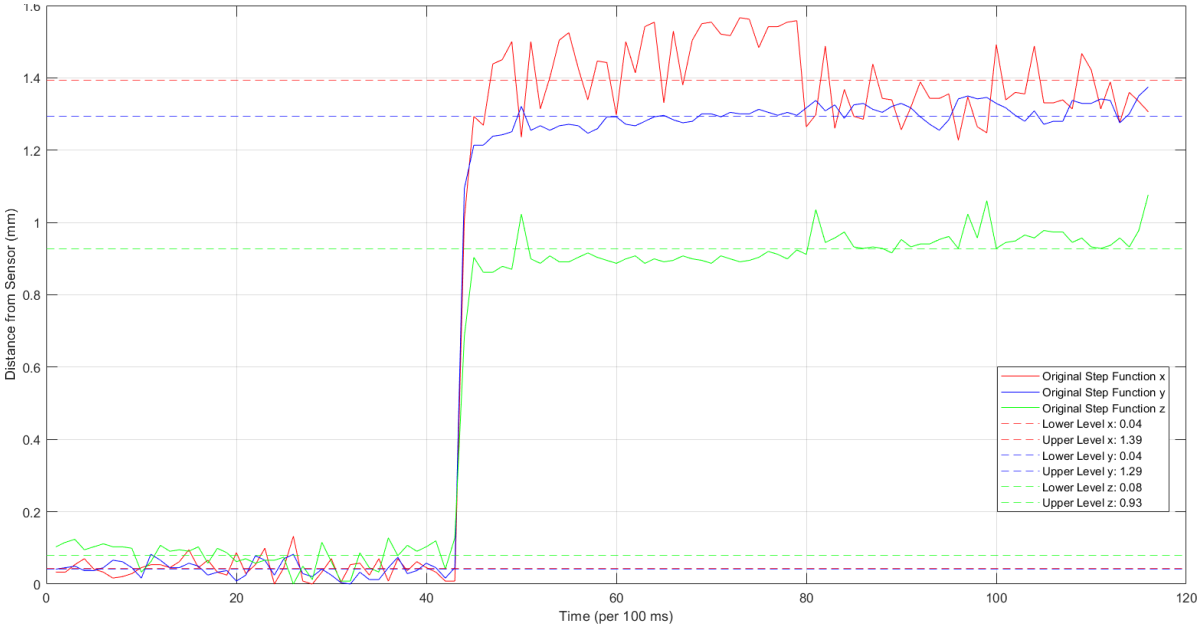

Figure 4.15: Step functions indicating the change in distance between each output point and their respective sensors, when a pressure of 0.1 MPa is internally applied. The difference between the lower and upper step limit is the total displacement occurred by the output face in the direction normal to it. The upper and lower limit of the step function was found using k-means clustering to divide the distance data into two groups [72].

The relative difference in values between the different design models are calculated and noted in Table 4.1.

	Value	Relative difference to Topology optimization	Relative difference to COMSOL study
Displacement obtained through topology optimization	-1.761 mm	—	—
Displacement obtained through COMSOL study	-1.437 mm	18.399%	—
Displacement obtained through experimental setup [13]	-1.301 mm	26.099%	9.436%

Table 4.1: Displacement values and their relative differences.

The main inference drawn from Table 4.1, is that a significant difference is observed between the displacement value found in TO and the displacement found through the COMSOL study. This is largely due to two main reasons. First, the density threshold selected while translating the TO-obtained design to an STL file. In the TO problem, the displacement value depends on all the elements in the design space, with each element contributing according to its modulus of elasticity, which is related to its elemental density. However, setting a threshold causes the influence of elements below the threshold to be lost while magnifying the influence of elements above the threshold. Second, the iso-curves created by the STL file results in a smoothed representation of the design. This smoothing can cause the loss of topological features or the creation of additional features, which affects the overall displacement value.

13 Average displacement of the horizontal displacements.

5

Conclusion and Future Scope

5.1. Conclusion

Through this study, a new systematic approach to the design of NLC metamaterials using density-based TO, is established. It can be easily implemented with the following steps:

1. Selecting the appropriate TO parameters, that depend on the unit cell size, its resolution, the material requirements and the boundary conditions.
2. Making appropriate design domain choices, that suits the application and satisfies the manufacturing process requirements. This includes selecting passive regions, planes of symmetry and location of output points.
3. Selecting an appropriate method to define pressure forces. The “Darcy Method” works for all cases, but one could also use the standard approach in design-independent cases for its ease of implementation and computation speed.
4. Selecting constraints, not only to satisfy application and manufacturing constraints, but also to focus on achieving or improving a certain aspect of the design, e.g., output displacement and stiffness.

Using TO with a CM formulation one is able to achieve isotropic NLC metamaterials, in two and three dimensions, both of which have been showcased through this study. This study shows that TO can not only take into account various constraints, such as volume fraction and strain energy but can also define passive regions/fixed topologies. Existing NLC design methodologies cannot accommodate these constraints and passive layouts that may be required by applications or manufacturing processes. These constraints, can also be used to achieve higher NLC values as shown in Section 4.6.2.

This study has also shown that through the CM formulation feasible results can be achieved, provided the correct regularization techniques are used and the right parameter values are selected. The “Darcy Method” has demonstrated its effectiveness when it comes to tackling pressure load problems in TO. While past literature has proven the “Darcy Method” to be superior to other existing pressure load application [56] method, a more simplistic approach of pressure load application can be used to tackle problems that are design-independent. This method is preferred because it is computationally inexpensive and easy to implement. This is inferred from the comparative study undertaken in Section 4.6.1.

The parameter study in Section 4.5 shows how certain TO parameters, such as volume fraction *f*, output spring stiffness k_{ss}, input pressure p_{in} and some passive region parameters including shape, defining length, and thickness, affect the final NLC value of the design. This demonstrates that a parameter study can help further optimize our design and advance the development of metamaterials with higher NLC values.

Lastly, the study proves that it is possible to translate this design to a CAD and real-world model without losing its NLC behavior. The relative difference between the design obtained using TO and the man-

ufactured design model is 26.099%, while the relative difference between the design obtained using TO and the CAD design model is 18.399% (these difference are observed in for the isotropic NLC unit cube design). There is scope for improvement in translating the TO-obtained design into CAD and real-world models, through better design-to-CAD translation and improved manufacturing techniques.

5.2. Future Scope

While this study has established TO as a foundational design process for engineering of NLC metamaterial unit cells, there remains room for further development. For instance:

1. A better understanding of how different TO parameters affect the final design. The parameter study in this research was limited a few parameters in the 2D case. This is because a parameter study involving more TO parameters or a 3D case study is computationally expensive.
2. Exploring the possibilities of porous designs in two and three dimensions. These designs are easier to manufacture, because they do not contain any enclosed parts that trap the fluid.[1]
3. Implementing geometric non-linearity, path following outputs and fixed output displacement values. These objectives could lead to better designs with larger NLC values and eliminate unwanted displacements, such as those in the x and y directions for an output point primarily moving along the z axis. These displacements can lead to twists in the metamaterial and undesired anisotropy in NLC values.
4. Exploring the implementation of different constraints tailored to real-world requirements, such as constraints on failure criteria, particularly fatigue. This constraint is crucial for ensuring the durability of metamaterials over multiple load cycles.
5. Developing anisotropic NLC designs is also a direction that can be explored. With the right constraints, objective functions and output stiffness, anisotropic designs could be achieved. One could also create an anisotropic design to compensate for the self weight induced load acting along the vertical axis thereby creating a more practical isotropic NLC metamaterial.

There is also future scope in the testing and manufacturing of the NLC unit cell designs obtained.

1. Array testing: While the unit cell designs display NLC behavior, an array of these unit cells is yet to be tested. The designs obtained through TO are complex and have limited the testing of these unit cells in an arrays. Better design translation techniques and/or a simplification of the designs obtained through TO can get rid of this limitation. Array testing is important as it helps us better understand how these unit cells interact with each other and also gives us a more realistic NLC value for the overall metamaterial.[2] If experimentally tested, it could also show us how manufacturing errors or inaccuracies could lead to problems or changes in NLC values as these errors are multiplied and more pronounced in an array.
2. Manufacturing on the microscopic scale: The unit cells of metamaterials are designed to be manufactured at the microscopic scale.[3] The scale does not affect the design or its NLC value, and the designs obtained in this study can be scaled down. However, manufacturing the obtained NLC unit cells at the microscopic scale poses challenges due to their complex shapes and the scale of manufacturing. Therefore, investigating various micro-scale manufacturing techniques capable of fabricating these unit cells is essential.

Overall, the complex NLC unit cell designs obtained coupled with the lack of research in suitable microscopic techniques limits our research to the design and testing of unit cells in the macroscopic scale. Although testing unit cells manufactured at the macroscopic level allows us to fairly accurately predict the overall metamaterial NLC behavior, the most accurate test would involve a large array of unit cells manufactured at the microscopic level.

1 Enclosed parts, such as the pressurized shell in the design-dependent case and the inner cube in the design-independent case, are difficult to manufacture using additive techniques, as they trap support material.
2 Section 4.6.2 shows us how the NLC value in a unit cell differs from that of an array.
3 Note: It is only possible to test the metamaterial at the macroscopic scale if its unit cells are manufactured in the microscopic scale.

References

[1] Wenlong Huang, Chenxia Li, Bo Fang, Jianfeng Xu, Fuhai Liu, Lizhen Xu, Ying Tang, Zhi Hong, and Xufeng Jing. “Research progress of terahertz wave dynamic control of digital coded metasurfaces”. In: *Optics and Lasers in Engineering* 174 (2024), p. 107977. ISSN: 0143-8166.

[2] Chuanwei Huang and Lang Chen. “Negative Poisson’s Ratio in Modern Functional Materials”. In: *Advanced Materials* 28.37 (2016), pp. 8079–8096. DOI: https://doi.org/10.1002/adma.201601363.

[3] João O. Cardoso, João Paulo Borges, and Alexandre Velhinho. “Structural metamaterials with negative mechanical/thermomechanical indices: A review”. In: *Progress in Natural Science: Materials International* 31.6 (2021), pp. 801–808. ISSN: 1002-0071. DOI: https://doi.org/10.1016/j.pnsc.2021.10.015.

[4] Xin Ren, Raj Das, Phuong Tran, Tuan Ngo, and Yi Xie. “Auxetic metamaterials and structures: A review”. In: *Smart Materials and Structures* 27 (Jan. 2018). DOI: 10.1088/1361-665X/aaa61c.

[5] Krishna Kumar Saxena, Raj Das, and Emilio P. Calius. “Three Decades of Auxetics Research − Materials with Negative Poisson’s Ratio: A Review”. In: *Advanced Engineering Materials* 18.11 (2016), pp. 1847–1870. DOI: https://doi.org/10.1002/adem.201600053.

[6] Cora Lind. “Two Decades of Negative Thermal Expansion Research: Where Do We Stand?” In: *Materials* 5.6 (2012), pp. 1125–1154. ISSN: 1996-1944. DOI: 10.3390/ma5061125.

[7] Ruben Gatt and Joseph N. Grima. “Negative compressibility”. In: *physica status solidi (RRL) - Rapid Research Letters* 2.5 (2008), pp. 236–238. DOI: https://doi.org/10.1002/pssr.200802101.

[8] Jingyuan Qu, Muamer Kadic, and Martin Wegener. “Three-dimensional poroelastic metamaterials with extremely negative or positive effective static volume compressibility”. In: *Extreme Mechanics Letters* 22 (2018), pp. 165–171. ISSN: 2352-4316. DOI: https://doi.org/10.1016/j.eml.2018.06.007.

[9] Ray H. Baughman, Sven Stafström, Changxing Cui, and Socrates O. Dantas. “Materials with Negative Compressibilities in One or More Dimensions”. In: *Science* 279.5356 (1998), pp. 1522–1524. DOI: 10.1126/science.279.5356.1522.

[10] P. W. Bridgman. “The Compressibility of Metals at High Pressures”. In: *Proceedings of the National Academy of Sciences* 8.12 (1922), pp. 361–365. DOI: 10.1073/pnas.8.12.361.

[11] Andrew B. Cairns and Andrew L. Goodwin. “Negative linear compressibility”. In: *Phys. Chem. Chem. Phys.* 17 (32 2015), pp. 20449–20465. DOI: 10.1039/C5CP00442J.

[12] W. Miller, K. E. Evans, and A. Marmier. “Negative linear compressibility in common materials”. In: *Applied Physics Letters* 106.23 (June 2015), p. 231903. ISSN: 0003-6951. DOI: 10.1063/1.4922460.

[13] Teik-Cheng Lim. *Mechanics of Metamaterials with Negative Parameters*. Jan. 2020. ISBN: 978-981-15-6445-1. DOI: 10.1007/978-981-15-6446-8.

[14] Xianglong Yu, Ji Zhou, Haiyi Liang, Zhengyi Jiang, and Lingling Wu. “Mechanical metamaterials associated with stiffness, rigidity and compressibility: A brief review”. In: *Progress in Materials Science* 94 (2018), pp. 114–173. ISSN: 0079-6425. DOI: https://doi.org/10.1016/j.pmatsci.2017.12.003.

[15] Larry L Howell. “Compliant mechanisms”. In: *21st century kinematics: The 2012 NSF Workshop*. Springer. 2013, pp. 189–216.

[16] Juan Gallego Sanchez and Just Herder. “Synthesis Methods in Compliant Mechanisms: An Overview”. In: vol. 7. Jan. 2009. DOI: 10.1115/DETC2009-86845.

[17] Martin Philip Bendsøe and Noboru Kikuchi. “Generating optimal topologies in structural design using a homogenization method”. In: *Computer Methods in Applied Mechanics and Engineering* 71.2 (1988), pp. 197–224. ISSN: 0045-7825. DOI: https://doi.org/10.1016/0045-7825(88)90086-2.

[18] Martin P. Bendsøe and Ole Sigmund. “Extensions and applications”. In: *Topology Optimization: Theory, Methods, and Applications*. Berlin, Heidelberg: Springer Berlin Heidelberg, 2004, pp. 71–158. ISBN: 978-3-662-05086-6. DOI: 10.1007/978-3-662-05086-6_2.

[19] Bastiaan Florijn, Corentin Coulais, and Martin van Hecke. “Programmable Mechanical Metamaterials”. In: *Phys. Rev. Lett.* 113 (17 Oct. 2014), p. 175503. DOI: 10.1103/PhysRevLett.113.175503.

[20] Ji-Xiang Qi, Zihao Chen, Peng Jiang, Wenxia Hu, Yonghuan Wang, Zeang Zhao, Xiaofei Cao, Shushan Zhang, Ran Tao, and Daining Fang. “Recent Progress in Active Mechanical Metamaterials and Construction Principles”. In: *Advanced Science* (Oct. 2021). DOI: 10.1002/advs.202102662.

[21] Jiao Jia, Jianxing Hu, Yongbin Wang, Shiqing Wu, and Long Kai. “Structural topology optimization with positive and negative Poisson’s ratio materials”. In: *Engineering Computations* ahead-of-print (Jan. 2020). DOI: 10.1108/EC-06-2019-0291.

[22] K. Dudek, D. Attard, R. Gatt, J.N. Grima-Cornish, and J.N. Grima. “The Multidirectional Auxeticity and Negative Linear Compressibility of a 3D Mechanical Metamaterial”. In: *Materials (Basel)* 13.9 (May 2020), p. 2193. DOI: 10.3390/ma13092193.

[23] Joseph Grima, Daphne Attard, and Ruben Gatt. “Truss-type systems exhibiting negative compressibility”. In: *physica status solidi (b)* 245 (Nov. 2008), pp. 2405–2414. DOI: 10.1002/pssb.200880267.

[24] Joseph N. Grima, Daphne Attard, Roberto Caruana-Gauci, and Ruben Gatt. “Negative linear compressibility of hexagonal honeycombs and related systems”. In: *Scripta Materialia* 65.7 (2011), pp. 565–568. ISSN: 1359-6462. DOI: https://doi.org/10.1016/j.scriptamat.2011.06.011.

[25] Joseph N. Grima, Ruth Caruana-Gauci, David Attard, and Ruben Gatt. “Three-dimensional cellular structures with negative Poisson’s ratio and negative compressibility properties”. In: *Proceedings of the Royal Society A* 468.2146 (2012), pp. 3121–3138. DOI: 10.1098/rspa.2012.0187.

[26] Joseph N Grima, Roberto Caruana-Gauci, Krzysztof W Wojciechowski, and Kenneth E Evans. “Smart hexagonal truss systems exhibiting negative compressibility through constrained angle stretching”. In: *Smart Materials and Structures* 22.8 (July 2013), p. 084015. DOI: 10.1088/0964-1726/22/8/084015.

[27] David Attard, Ruth Caruana-Gauci, Ruben Gatt, and Joseph N. Grima. “Negative linear compressibility from rotating rigid units”. In: *Physica Status Solidi (b)* 253.7 (2016), pp. 1410–1418. DOI: 10.1002/pssb.201600123.

[28] Xiaoqing Zhou, Lei Zhang, Huan Zhang, Qian Liu, and Ting Ren. “3D cellular models with negative compressibility through the wine-rack-type mechanism”. In: *Physica Status Solidi (b)* 253.10 (2016), pp. 1977–1993. DOI: 10.1002/pssb.201600187.

[29] X. Zhou, J. Li, M. Ma, and L. Yang. “The comparison of negative linear compressibility of hexagonal honeycomb under different layouts”. In: *IOP Conference Series: Materials Science and Engineering* 394.3 (2018), p. 032076. DOI: 10.1088/1757-899X/394/3/032076.

[30] M. Ma, X. Zhou, J. Li, H. Li, and S. He. “The negative compressibility in 3D cellular elongated octahedron model”. In: *IOP Conference Series: Earth and Environmental Science* 252.2 (2019), p. 022140. DOI: 10.1088/1755-1315/252/2/022140.

[31] Katarzyna K. Dudek, David Attard, Ruth Caruana-Gauci, Krzysztof W. Wojciechowski, and Joseph N. Grima. “Unimode metamaterials exhibiting negative linear compressibility and negative thermal expansion”. In: *Smart Materials and Structures* 25.2 (2016), p. 025009. DOI: 10.1088/0964-1726/25/2/025009.

[32] Joseph N. Grima-Cornish, Joseph N. Grima, and David Attard. “A novel mechanical metamaterial exhibiting auxetic behavior and negative compressibility”. In: *Materials* 13.1 (2020), p. 79. DOI: 10.3390/ma13010079.

[33] Jingyuan Qu, Kadic Muamer, and Martin Wegener. “Poroelastic metamaterials with negative effective static compressibility”. In: *Applied Physics Letters* 110 (Apr. 2017), p. 171901. DOI: 10.1063/1.4981783.

[34] Ole Sigmund. “Design of Material Structures Using Topology Optimization”. PhD thesis. Jan. 1994.

[35] Alexandra Ion, David Lindlbauer, Philipp Herholz, Marc Alexa, and Patrick Baudisch. “Understanding Metamaterial Mechanisms”. In: *Proceedings of the 2019 CHI Conference on Human*

Factors in Computing Systems. CHI '19. Glasgow, Scotland Uk: Association for Computing Machinery, 2019, pp. 1–14. ISBN: 9781450359702. DOI: 10.1145/3290605.3300877.

[36] Kwangwon Kim and Jaehyung Ju. "Mechanical metamaterials with 3D compliant porous structures". In: *Composite Structures* 132 (2015), pp. 874–884. ISSN: 0263-8223. DOI: https://doi.org/10.1016/j.compstruct.2015.06.060.

[37] G. K. Ananthasuresh, S. Kota, and Y. Gianchandani. "A Methodical Approach to the Design of Compliant Micromechanisms". In: *Solid-State Sensor and Actuator Workshop*. 1994, pp. 189–192.

[38] Ole Sigmund. "Some Inverse Problems in Topology Design of Materials and Mechanisms". In: *Symposium on Optimization of Mechanical Systems*. Ed. by D. Bestle and W. Schielen. IUTAM. Netherlands: Kluwer, 1996, pp. 277–284.

[39] G. K. Ananthasuresh, S. Kota, and N. Kikuchi. "Strategies for Systematic Synthesis of Compliant MEMS". In: *Dynamic Systems and Control* 2 (1994), pp. 677–686.

[40] Ole Sigmund. *Systematic Design of Metamaterials by Topology Optimization*. Springer, 2015. ISBN: 978-3-319-08954-2.

[41] Ulrik Darling Larsen, Ole Sigmund, and Siebe Bouwstra. "Design and Fabrication of Compliant Micromechanisms and Structures with Negative Poisson's Ratio". In: *Journal of Microelectromechanical Systems* 24.1 (2015), pp. 77–84. DOI: 10.1109/JMEMS.2014.2343974.

[42] Ole Sigmund. "On the Design of Compliant Mechanisms Using Topology Optimization". In: *Mechanics of Structures and Machines* 25.4 (1997), pp. 493–524.

[43] M. I. Frecker, G. K. Ananthasuresh, S. Nishiwaki, N. Kikuchi, and S. Kota. "Topological Synthesis of Compliant Mechanisms Using Multi-Criteria Optimization". In: *Journal of Mechanical Design* 119.2 (June 1997), pp. 238–245. ISSN: 1050-0472. DOI: 10.1115/1.2826242.

[44] V.B. Hammer and N. Olhoff. "Topology optimization of continuum structures subjected to pressure loading". In: *Structural and Multidisciplinary Optimization* 19 (Apr. 2000), pp. 85–92. DOI: 10.1007/s001580050088.

[45] J. Du and N. Olhoff. "Topological Optimization of Continuum Structures with Design-Dependent Surface Loading - Part I: New Computational Approach for 2D Problems". In: *Structural and Multidisciplinary Optimization* 27.3 (2004), pp. 151–165. DOI: 10.1007/s00158-004-0426-8.

[46] B. Zheng, C. J. Chang, and H. C. Gea. "Topology Optimization with Design-Dependent Pressure Loading". In: *Structural and Multidisciplinary Optimization* 38.6 (2009), pp. 535–543. DOI: 10.1007/s00158-008-0340-1.

[47] E. Lee and J. R. R. A. Martins. "Structural Topology Optimization with Design-Dependent Pressure Loads". In: *Computer Methods in Applied Mechanics and Engineering* 233–236 (2012), pp. 40–48. DOI: 10.1016/j.cma.2012.03.017.

[48] M. B. Fuchs and N. N. Y. Shemesh. "Density-Based Topological Design of Structures Subjected to Water Pressure Using a Parametric Loading Surface". In: *Structural and Multidisciplinary Optimization* 28.1 (2004), pp. 11–19. DOI: 10.1007/s00158-003-0366-6.

[49] Z. M. Li, J. Yu, Y. Yu, and L. Xu. "Topology Optimization of Pressure Structures Based on Regional Contour Tracking Technology". In: *Structural and Multidisciplinary Optimization* 58.2 (2018), pp. 687–700. DOI: 10.1007/s00158-018-1986-9.

[50] O. Sigmund and P.M. Clausen. "Topology optimization using a mixed formulation: An alternative way to solve pressure load problems". In: *Computer Methods in Applied Mechanics and Engineering* 196.13 (2007), pp. 1874–1889. ISSN: 0045-7825. DOI: https://doi.org/10.1016/j.cma.2006.09.021.

[51] B. C. Chen and N. Kikuchi. "Topology Optimization with Design-Dependent Loads". In: *Finite Elements in Analysis and Design* 37.1 (2001), pp. 57–70. DOI: 10.1016/S0168-874X(00)00054-4.

[52] B. Bourdin and A. Chambolle. "Design-Dependent Loads in Topology Optimization". In: *ESAIM: Control, Optimisation and Calculus of Variations* 9 (2003), pp. 19–48. DOI: 10.1051/cocv:2002062.

[53] H. Zhang, X. Zhang, and S. T. Liu. "A New Boundary Search Scheme for Topology Optimization of Continuum Structures with Design-Dependent Loads". In: *Structural and Multidisciplinary Optimization* 37.2 (2008), pp. 121–129. DOI: 10.1007/s00158-008-0255-y.

[54] S. Vasista and L. Tong. "Design and Testing of Pressurized Cellular Planar Morphing Structures". In: *AIAA Journal* 50.6 (2012), pp. 1328–1338. DOI: 10.2514/1.J051889.

[55] H. Panganiban, G. W. Jang, and T. J. Chung. “Topology Optimization of Pressure-Actuated Compliant Mechanisms”. In: *Finite Elements in Analysis and Design* 46.3 (2010), pp. 238–246. DOI: 10.1016/j.finel.2009.10.005.

[56] Prabhat Kumar, J. Frouws, and Matthijs Langelaar. “Topology optimization of fluidic pressure-loaded structures and compliant mechanisms using the Darcy method”. In: *Structural and Multidisciplinary Optimization* 61 (Apr. 2020), pp. 1–19. DOI: 10.1007/s00158-019-02442-0.

[57] Prabhat Kumar and Matthijs Langelaar. “Topological synthesis of fluidic pressure-actuated robust compliant mechanisms”. In: *Mechanism and Machine Theory* 174 (2022), p. 104871. ISSN: 0094-114X. DOI: https://doi.org/10.1016/j.mechmachtheory.2022.104871.

[58] Prabhat Kumar. “SoRoTop: a hitchhiker’s guide to topology optimization MATLAB code for design-dependent pneumatic-driven soft robots”. In: *Optimization and Engineering* (Nov. 2023). DOI: 10.1007/s11081-023-09865-1.

[59] K. Svanberg. “The Method of Moving Asymptotes – A New Method for Structural Optimization”. In: *International Journal for Numerical Methods in Engineering* 24 (1987), pp. 359–373. DOI: 10.1002/nme.1620240207.

[60] Prabhat Kumar. “TOPress: a MATLAB implementation for topology optimization of structures subjected to design-dependent pressure loads”. In: *Structural and Multidisciplinary Optimization* 66 (Apr. 2023). DOI: 10.1007/s00158-023-03533-9.

[61] A. Saxena and G. Ananthasuresh. “On an Optimal Property of Compliant Topologies”. In: *Structural and Multidisciplinary Optimization* 19.1 (2000), pp. 36–49. DOI: 10.1007/s001580050115.

[62] G. Batchelor. *An Introduction to Fluid Dynamics*. Cambridge: Cambridge University Press, 2000.

[63] Prabhat Kumar and Matthijs Langelaar. “On topology optimization of design-dependent pressure-loaded three-dimensional structures and compliant mechanisms”. In: *International Journal for Numerical Methods in Engineering* 122.9 (2021), pp. 2205–2220. DOI: https://doi.org/10.1002/nme.6618.

[64] Martin P. Bendsøe and Ole Sigmund. “Topology optimization by distribution of isotropic material”. In: *Topology Optimization: Theory, Methods, and Applications*. Berlin, Heidelberg: Springer Berlin Heidelberg, 2004, pp. 1–69. ISBN: 978-3-662-05086-6. DOI: 10.1007/978-3-662-05086-6_1.

[65] A. Díaz and O. Sigmund. “Checkerboard Patterns in Layout Optimization”. In: *Structural Optimization* 10.1 (1995), pp. 40–45. DOI: 10.1007/BF01197744.

[66] C. Jog and R. Haber. “Stability of Finite Element Models for Distributed-Parameter Optimization and Topology Design”. In: *Computer Methods in Applied Mechanics and Engineering* 130.3-4 (1996), pp. 203–226. DOI: 10.1016/0045-7825(95)00894-2.

[67] O. Sigmund and J. Petersson. “Numerical Instabilities in Topology Optimization: A Survey on Procedures Dealing with Checkerboards, Mesh-Dependencies, and Local Minima”. In: *Structural Optimization* 16.1 (1998), pp. 68–75. DOI: 10.1007/s001580050061.

[68] T. E. Bruns and D. A. Tortorelli. “Topology Optimization of Non-linear Elastic Structures and Compliant Mechanisms”. In: *Computer Methods in Applied Mechanics and Engineering* 190.26-27 (2001), pp. 3443–3459. DOI: 10.1016/S0045-7825(00)00386-2.

[69] B. Bourdin. “Filters in Topology Optimization”. In: *International Journal for Numerical Methods in Engineering* 50.9 (2001), pp. 2143–2158. DOI: 10.1002/1097-0207(20010210)50:9<2143::AID-NME268>3.0.CO;2-9.

[70] Jun Wu, Christian Dick, and Rüdiger Westermann. “A System for High-Resolution Topology Optimization”. In: *IEEE Transactions on Visualization and Computer Graphics* 22.3 (2016), pp. 1195–1208. DOI: 10.1109/TVCG.2015.2502588.

[71] Ole Sigmund. “Morphology-based black and white filters for topology optimization”. In: *Structural and Multidisciplinary Optimization* 33 (Apr. 2007), pp. 401–424. DOI: 10.1007/s00158-006-0087-x.

[72] S. Lloyd. “Least squares quantization in PCM”. In: *IEEE Transactions on Information Theory* 28.2 (1982), pp. 129–137. DOI: 10.1109/TIT.1982.1056489.